

Interaction of sortilin with apolipoprotein E3 enables neurons to use long-chain fatty acids as alternative metabolic fuel

Received: 20 June 2024

Accepted: 5 September 2025

Published online: 16 October 2025

 Check for updates

Anna K. Greda^{1,10}, Jemila P. Gomes^{1,2,10}, Vanessa Schmidt-Krueger², Ewa Zurawska-Plaksej^{2,3}, Raphaela Fritsche-Guenther⁴, Ina-Maria Rudolph², Narasimha S. Telugu⁵, Cagla Cömert⁶, Jennifer Kirwan⁴, Séverine Kunz⁷, Michael Rothe⁸, Mogens Johannsen⁹, Sebastian Diecke⁵, Peter Bross⁶ & Thomas E. Willnow^{1,2}✉

Sortilin (*SORT1*) is a lipoprotein receptor that shows genome-wide association with hypercholesterolaemia, explained by its ability to control hepatic output of lipoproteins. Although *SORT1* also shows genome-wide association with Alzheimer disease and frontotemporal lobe dementia, the most prevalent forms of age-related dementias, sortilin's contribution to human brain lipid metabolism and health remains unclear. Here we show that sortilin mediates neuronal uptake of polyunsaturated fatty acids carried by apolipoprotein E (apoE). Using humanized mouse strains and induced pluripotent stem cell-based cell models of brain lipid homeostasis, we demonstrate that internalized lipids are converted into ligands for peroxisome proliferator-activated receptor alpha inducing transcription profiles that enable neurons to use long-chain fatty acids as metabolic fuel when glucose is limited. This pathway works with apoE3 but cannot operate with the Alzheimer disease risk factor apoE4, which disrupts sortilin's endocytic activity. Our data indicate a role for the lipoprotein receptor sortilin in metabolic fuel choice in neurons, which may be crucial when glucose supply is limited, such as in the ageing brain.

Sortilin is a 95-kDa type-1 transmembrane receptor expressed in various mammalian cell types, most notably in neurons of the central and peripheral nervous system and in hepatocytes in the liver^{1–3}. Sortilin operates as an endocytic and intracellular sorting receptor, directing cargo between the cell surface and various compartments of biosynthetic and endocytic pathways (reviewed in refs. 4–6). In the liver, it acts as a lipoprotein receptor controlling hepatic uptake but also release of cholesterol-rich lipoproteins, explaining genome-wide association of

the encoding gene *SORT1* with plasma cholesterol levels and the risk of myocardial infarction^{2,3,7–9}

Recently, we showed that sortilin also acts as a lipoprotein receptor in the brain, facilitating neuronal uptake of apolipoprotein E (apoE), the major carrier for lipids in brain interstitial fluids¹⁰. ApoE is secreted by astrocytes and microglia and delivers essential lipids to neurons (reviewed in refs. 11–13). In mouse models, sortilin-dependent uptake of lipids works well with apoE3, the most common isoform of the lipid

¹Department of Biomedicine, Aarhus University, Aarhus, Denmark. ²Molecular Cardiovascular Research, Max-Delbrueck-Center for Molecular Medicine in the Helmholtz Association, Berlin, Germany. ³Department of Toxicology, Wroclaw Medical University, Wroclaw, Poland. ⁴Berlin Institute of Health at Charité – Universitätsmedizin Berlin, Metabolomics, Berlin, Germany. ⁵Technology Platform for Pluripotent Stem Cells, Max-Delbrueck-Center for Molecular Medicine in the Helmholtz Association, Berlin, Germany. ⁶Department of Clinical Medicine, Aarhus University, Aarhus, Denmark. ⁷Technology Platform for Electron Microscopy, Max-Delbrueck-Center for Molecular Medicine in the Helmholtz Association, Berlin, Germany. ⁸Lipidomix GmbH, Berlin, Germany. ⁹Department of Forensic Medicine, Aarhus University, Aarhus, Denmark. ¹⁰These authors contributed equally: Anna K. Greda, Jemila P. Gomes.

✉e-mail: tew@biomed.au.dk

carrier in humans. However, this function of sortilin is disrupted when binding lipidated apoE4, as this apoE variant blocks sortilin recycling and ceases receptor-mediated ligand uptake into cells^{14,15}. This observation is important as *APOE* ϵ 4 represents the major genetic risk factor for sporadic Alzheimer disease, increasing disease risk in homozygous carriers by 12-fold as compared to carriers of the common *APOE* ϵ 3/ ϵ 3 genotype¹⁶.

So far, the physiological relevance of sortilin-mediated neuronal uptake of lipids in the human brain remains unclear. However, such functions may well provide a molecular explanation for the genome-wide association of *SORT1* with both Alzheimer disease¹⁷ and frontotemporal lobe dementia (FTD)¹⁸, the two most common forms of age-dependent neurodegeneration in the human population. Here, we used humanized mouse strains and induced pluripotent stem (iPS) cell-derived cell models to recapitulate aspects of the human brain lipid metabolism *in vivo* and *in vitro* and to elucidate the relevance of sortilin-dependent lipid homeostasis for neuronal health. Our studies identified a unique metabolic concept whereby apoE-bound polyunsaturated fatty acids (PUFAs) internalized by sortilin are converted into ligands for peroxisome proliferator-activated receptor (PPAR) α , a key transcriptional regulator of enzymes involved in the use of long-chain fatty acids (LCFAs) as metabolic fuel for mitochondrial energy production¹⁹. This sortilin pathway is essential to sustain neuronal energy homeostasis when use of glucose is limited, and it is lost in the presence of apoE4 that disrupts sortilin's function as a neuronal lipoprotein receptor.

Results

Loss of sortilin or the presence of apoE4 impairs the respiratory capacity of neurons

To interrogate the relevance of sortilin and apoE interactions for brain lipid metabolism *in vivo*, we studied mouse strains carrying a targeted replacement of the mouse *ApoE* locus with genes encoding human apoE3 (E3) or apoE4 (E4)²⁰. In addition, the animals were either wild-type (WT) or genetically deficient (knockout, KO) for *Sort1* (refs. 1,14). When exploring possible metabolic phenotypes related to the interaction of sortilin with apoE, we focused on possible traits distinct in E3WT mice as compared to the other three genotypes (that is, E3KO, E4WT and E4KO). This strategy was based on our hypothesis that interaction of sortilin with apoE3 in E3WT animals sustains proper metabolism and actions of lipids (Fig. 1a). However, these lipid pathways will be lost in E3 mice genetically deficient for sortilin (E3KO). The same phenotypes as in E3KO should be seen in E4 animals, regardless of being WT or KO for *Sort1*, as these mouse models are either functional (E4WT) or genetically deficient (E4KO) for sortilin activity¹⁵ (Fig. 1a).

Given the documented impact of sortilin on apoE-dependent lipid homeostasis in the mouse brain^{10,14}, we investigated genotype-specific consequences for neuronal energy homeostasis using real-time measurement of mitochondrial respiration (Seahorse Technology, Agilent).

To specifically assess neuronal respiration, we isolated synaptosomes from brain cortices of our four mouse strains. Synaptosomes are a source of neuronal mitochondria, entrapped during preparation from brain tissue by density gradient ultracentrifugation²¹. The presence of neuronal but absence of astrocytic marker proteins confirmed the purity of our synaptosomal preparations (Extended Data Fig. 1a). Comparing mitochondrial oxygen consumption rates (OCRs) in the presence of normal glucose levels, we identified a significantly higher maximal respiration in E3WT as compared to E3KO, E4WT or E4KO synaptosomes, with no statistically significant differences between the latter three genotypes (Fig. 1b,d and Supplementary Fig. 1). Other mitochondrial parameters, including basal respiration (Fig. 1c), proton leak (Fig. 1e) or ATP-linked respiration (Fig. 1f) did not show such interaction of genotypes. Also, western blot analysis of synaptosomal extracts as well as morphometric analysis of electron microscopy images of purified synaptosomes did not reveal any discernible differences in mitochondrial protein content (Extended Data Fig. 1b) or structural appearance of these organelles (mitochondrial area and circularity; Extended Data Fig. 1c,d) indicative of genotype interaction.

Genetic or functional sortilin deficiency blocks the ability of mouse neurons to use LCFAs as metabolic fuel

To test whether metabolic fuel choices may distinguish E3WT from E3KO and E4 synaptosomes, we performed a substrate oxidation stress test by treating synaptosomes with UK5099 or etomoxir in the presence of normal glucose levels. UK5099 targets the mitochondrial pyruvate carrier, blocking the ability of mitochondria to use pyruvate derived from glycolysis as fuel²². Etomoxir is an inhibitor of CPT1A, disrupting mitochondrial import of LCFAs²³. Treatment of E3WT synaptosomes with UK5099 or etomoxir significantly reduced maximal respiration as compared to solvent-treated samples (Fig. 1g and Supplementary Fig. 2a), documenting the ability of neuronal mitochondria from E3WT to use both glucose and LCFAs as energetic fuel. By contrast, synaptosomal mitochondria from E3KO (Fig. 1h and Supplementary Fig. 2b), E4WT (Fig. 1i and Supplementary Fig. 2c) and E4KO (Fig. 1j and Supplementary Fig. 2d) were sensitive to treatment with UK5099 but failed to respond to etomoxir. Insensitivity to etomoxir, as seen in synaptosomes from male mice in Fig. 1h–j, was also observed in synaptosomes isolated from female animals (Extended Data Fig. 2 and Supplementary Fig. 3). These findings documented an inability of E3KO and E4 genotypes to utilize LCFAs as fuel for mitochondrial energy production. The inability to consume LCFAs was further addressed by testing whether synaptosomes were able to respire when glucose was depleted but the LCFA palmitate was added as an alternative fuel. In these experiments, mitochondrial respiration sustained in E3WT synaptosomes, but shut down completely in the three other genotypes, possibly impacting overall cell viability and (mitochondrial) functions even further (Fig. 2a).

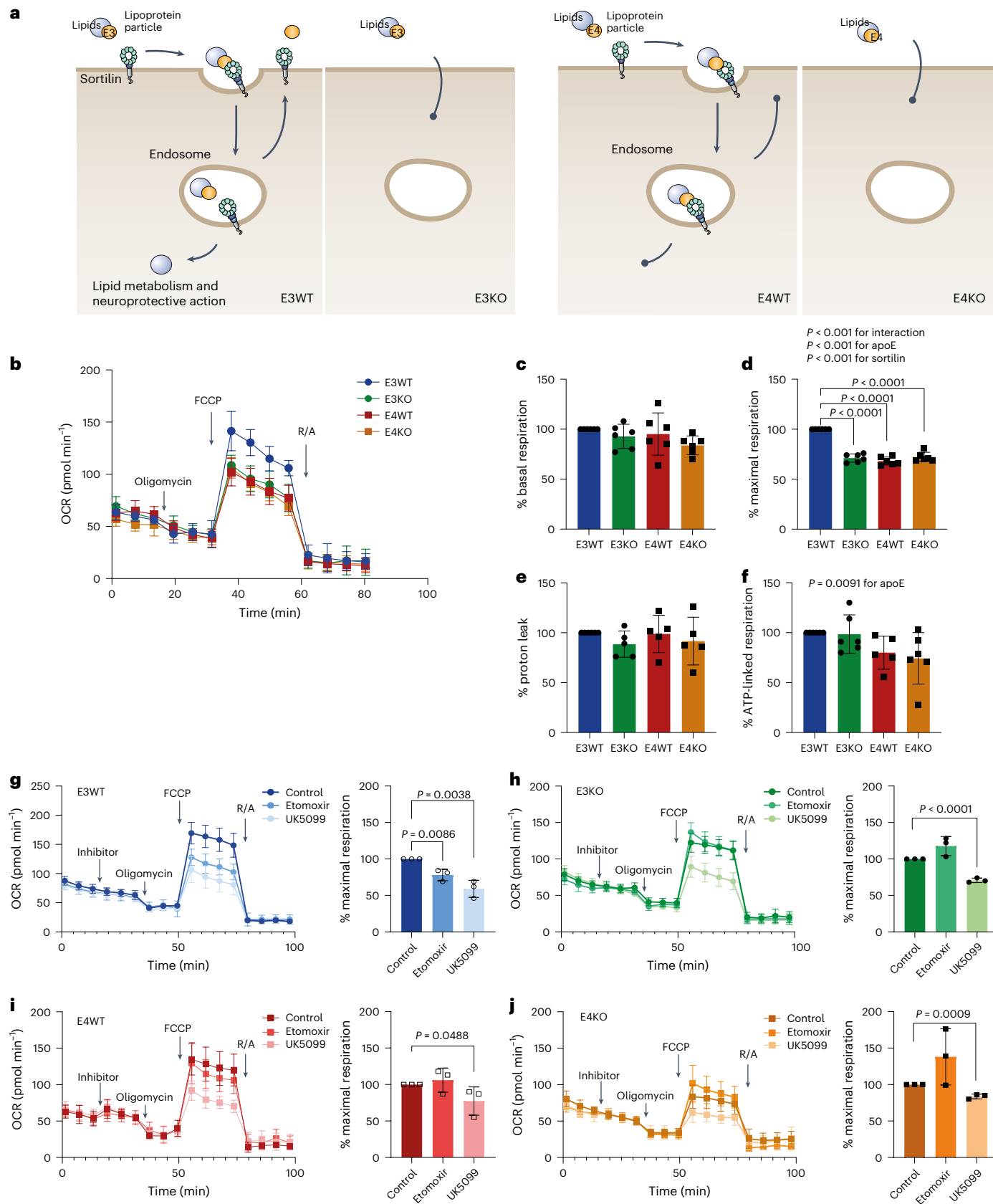
To further characterize the impact of genotypes on lipid fuel use, we performed real-time measurement of mitochondrial respiration

Fig. 1 | Loss of sortilin or the presence of apoE4 renders neuronal mitochondria insensitive to inhibition of LCFA import. **a**, Proposed model of sortilin and apoE isoform-specific interactions in neuronal lipid handling. Normal receptor function in cellular lipid homeostasis is seen in WT mice expressing apoE3 (E3WT), governing cellular uptake and neuroprotective metabolism and action of essential lipids. Functional (E4WT) or genetic (E3KO, E4KO) sortilin deficiency disrupts neuronal uptake and metabolism of such lipids in the other three genotypes. **b**, Quantification of real-time cellular OCR in synaptosomes isolated from brain cortices of male mice of the indicated *Sort1* and *APOE* genotypes (12 weeks of age). Representative respiration profiles of E3WT, E3KO, E4WT and E4KO synaptosomes are given. OCR was measured under basal conditions (0–20 min) and following sequential addition of oligomycin, carbonyl cyanide-p-trifluoromethoxyphenylhydrazone (FCCP), and rotenone and antimycin A (R/A) at the indicated time points. Respiration profiles of all six independent experiments are given in Supplementary Fig. 1. **c–f**, Quantification of basal respiration (**c**), maximal respiration (**d**), proton leak (**e**) and ATP-linked

respiration (**f**) in synaptosomes of the indicated genotypes relative to E3WT (set to 100%). Data are given as the mean \pm s.d. of $n = 5–6$ biological replicates (mice) per genotype group. Each biological replicate data point is the mean of $n = 18–24$ technical replicates. Statistical significance was tested using two-way analysis of variance (ANOVA) with Tukey's multiple-comparison test. **g–j**, The dependency of mitochondrial respiration on availability of glucose or LCFAs was assessed as described under **b** in the presence of solvent control buffer (control) or solutions containing 8 μ M UK5099 or 16 μ M etomoxir (inhibitor). For each genotype, one exemplary experiment is shown (to the left) as well as the quantification of the percentage of maximal respiration compared to the control condition (set to 100%; to the right). Data are given as the mean \pm s.d. from $n = 3$ biological replicates. Each biological replicate data point is the mean of $n = 10–18$ technical replicates. Statistical significance was tested using an unpaired Student's *t*-test (two-tailed). Respiration profiles of all three independent experiments are given in Supplementary Fig. 2.

in synaptosomes substituted with long-, medium- or short-chain fatty acids. Only LCFAs require the carnitine shuttle system, whereas short-chain fatty acids (SCFAs) and medium-chain fatty acids (MCFAs) can pass the mitochondrial membranes. These studies were performed

under conditions of limited supply with glucose (20% of normal assay condition) and pyruvate (10% of normal assay condition) to mimic brain glucose hypometabolism. Maximal respiration increased in E3WT synaptosomes when substituted with palmitate (Fig. 2b and



Supplementary Fig. 4a). No increase in maximal respiration was seen in E3KO (Fig. 2c and Supplementary Fig. 4b), E4WT (Fig. 2d and Supplementary Fig. 4c) or E4KO (Fig. 2e and Supplementary Fig. 4d) synaptosomes after palmitate supplementation. The situation was different when glucose-deprived synaptosomes were provided with SCFAs as metabolic fuel. Addition of either acetic acid or butyric acid significantly increased maximal respiration in E3KO (Fig. 2g and Supplementary Fig. 5b), E4WT (Fig. 2h and Supplementary Fig. 5c) and E4KO (Fig. 2i and Supplementary Fig. 5d), whereas no effect was seen in E3WT (Fig. 2f and Supplementary Fig. 5a). We also tested the impact of the MCFA heptanoic acid and octanoic acid, used in treatment of patients with inherited deficiencies of mitochondrial import and oxidation of LCFA²⁴. MCFAs increased maximal respiration, an effect seen in all four genotypes (Fig. 2j–m and Supplementary Fig. 6). This observation indicated that the reduced ability of E3KO and E4 synaptosomes to use fatty acids as fuel was restricted to LCFAs requiring transport by the carnitine shuttle.

To corroborate that the differential impact of palmitate on OCR was explained by the ability of WT, but not sortilin-deficient, neurons to use LCFAs as an energy substrate, we measured tricarboxylic acid cycle (TCA) intermediates in E3WT and E3KO synaptosomes in the presence or absence of palmitate. Again, to mimic brain glucose hypometabolism, the assay was performed in medium containing reduced levels of glucose (20% of normal assay conditions) and pyruvate (10% of normal assay conditions). As documented by liquid chromatography–tandem mass spectrometry (LC–MS/MS)-based metabolomics, supplementation with palmitate increased the concentrations of citrate, malate and fumarate in E3WT synaptosomes (Extended Data Fig. 3a), an effect not seen in E3KO (Extended Data Fig. 3b).

Sortilin and apoE3 interact in transcriptional control of neuronal fatty acid metabolism in the mouse brain

To elucidate the molecular mechanisms underlying the inability of E3KO or E4 neurons to use LCFAs for respiration, we first quantified transcript levels of genes implicated in fatty acid metabolism and mitochondrial lipid consumption in mouse brain cortices. No interactions between *APOE* and *Sort1* genotypes were seen whereby transcript levels in E3WT would be significantly different from those in the other three genotypes (Extended Data Fig. 4). These findings argued that disrupted interactions of sortilin with apoE did not impact global brain lipid handling. The situation was different when we compared transcript levels in astrocytes and neurons individually sorted from brain cortices of the four genotypes. Purity of our cell preparations was confirmed by the exclusive presence of neuronal marker transcripts *NeuN/Rbfox3* (*NeuN*) and *Baf53b/Actl6b* (*Baf53b*) in sorted neurons (Fig. 3a) and astrocyte marker transcripts *Aldh1l1* and *Gfap* in sorted astrocytes (Fig. 3b). Some apoE genotype-dependent transcriptional changes were observed in astrocytes (*Slc16a1*, *Cpt2* and *Acadl*; Fig. 3c), in line with the established impact of apoE variants on astrocyte metabolism²⁵. However, an interaction of *APOE* and *Sort1* genotypes on transcript levels was only seen in neurons and included the fatty acid oxidation enzyme long-chain acyl-CoA dehydrogenase *Acadl*, and the carnitine acyltransferases *Crat* and *Cpt1a* (Fig. 3c).

The impact on neuronal expression of *Cpt1a* was particularly noteworthy as this gene encodes one of the components of the mitochondrial carnitine shuttle and pharmacological target of etomoxir²³. Apparently, sortilin and apoE3 interactions distinctly affected the fatty acid metabolism in neurons, but not astrocytes, a finding in line with the predominant neuronal expression of the receptor²⁶.

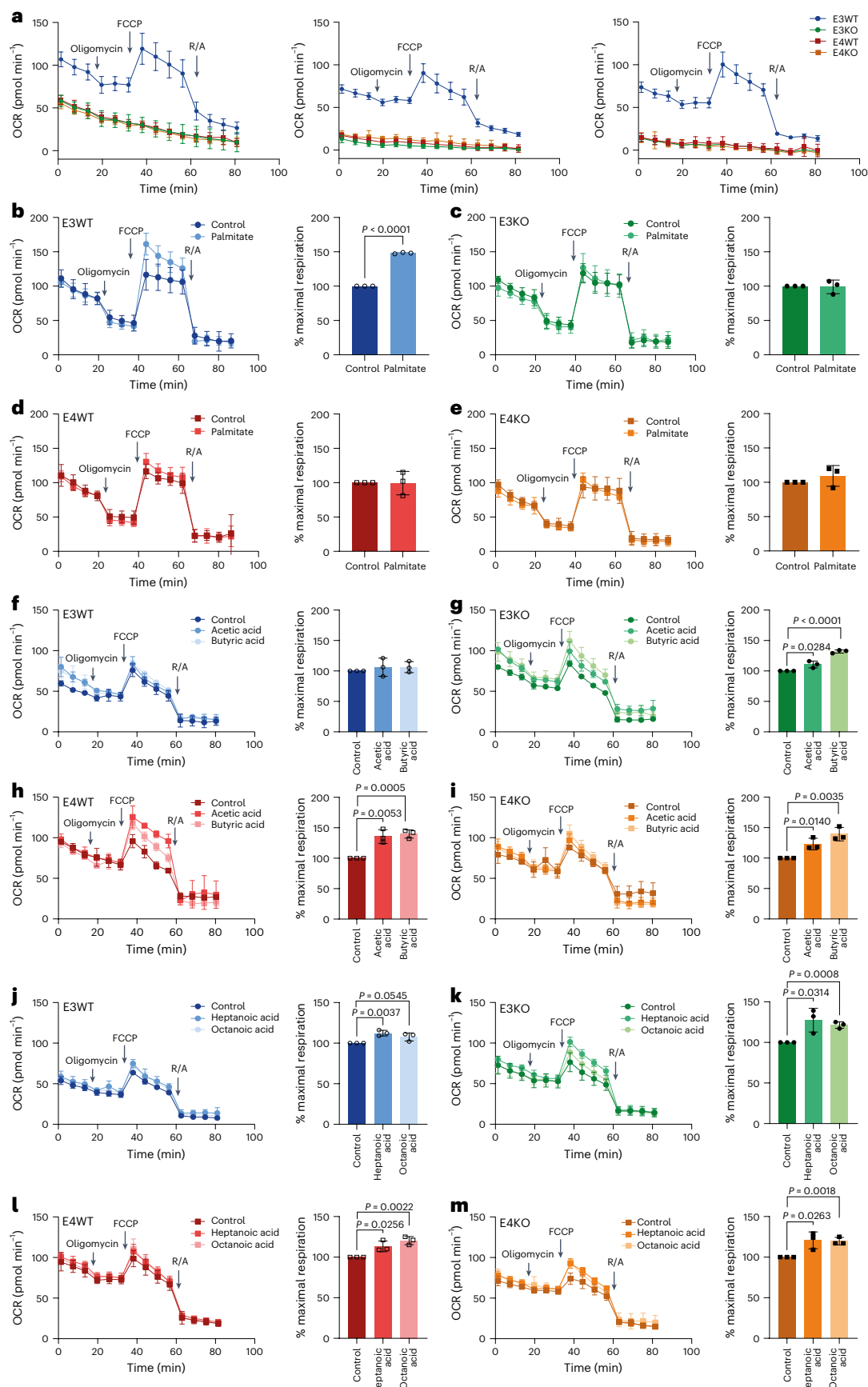
iPS cell-derived cell models recapitulate sortilin and apoE interactions in human brain lipid homeostasis

Next, we established iPS cell-based cell models to recapitulate neuron–astrocyte interactions in human brain lipid homeostasis. To this end, we used endonuclease-based strategies to introduce *SORT1* gene defects into human iPS cell lines homozygous for *APOE* ϵ 3 or *APOE* ϵ 4 (Supplementary Fig. 7a,b). Loss of sortilin expression was confirmed by western blotting (Supplementary Fig. 7c). *APOE* and *SORT1* genotypes did not impact pluripotency of the iPS cell lines as shown by testing expression of pluripotency markers using immunocytochemistry (Supplementary Fig. 7e,f) and quantitative PCR with reverse transcription (RT–qPCR; Supplementary Fig. 7d,g,h). To recapitulate cell-type-specific interactions in human brain lipid homeostasis, we differentiated the four iPS cell lines into astrocytes using an established protocol of retroviral-induced overexpression of *SOX9* and *NFIB*²⁷. The viral constructs also encoded mCherry to trace transduced cells (Extended Data Fig. 5a). All four genotypes generated astrocytes (referred to herein as induced astrocytes, iAs) that were comparable in appearance as well as in expression of astrocyte markers glial fibrillary acid protein (GFAP) and S100 β , as documented by immunocytochemistry (Extended Data Fig. 5b) and RT–qPCR (Extended Data Fig. 5c). Minor differences were seen in transcript levels for S100 β and aldehyde dehydrogenase family member L1 (ALDH1), but these changes did not show an interaction between *APOE* and *SORT1* genotypes (Extended Data Fig. 5c). Importantly, iAs of all four genotypes produced and secreted similar amounts of apoE variants as shown by comparative RT–qPCR (Extended Data Fig. 5c) and western blotting (Extended Data Fig. 5d).

In parallel, all four iPS cell lines were differentiated into cortical neurons using virus-induced expression of *NEUROG2* (*NGN2*)²⁸. In addition, the retroviral constructs also encoded GFP as a transduction marker. To avoid the presence of glia in our neuronal cultures, we adapted the neuronal differentiation protocol by adding media conditioned by human iAs instead of mouse glia (Extended Data Fig. 5g,h). This protocol reliably produced iPS cell-derived neurons from all four genotypes (referred to as induced neurons, iNs), comparable in cellular appearance and neuronal marker expression to neurons differentiated using the standard astrocyte co-culture protocol (Extended Data Fig. 5e,f). No discernible genotype-dependent differences in expression of neuronal markers MAP2 as well TUJ1 (TUBB3), neurofilament light chain (NEFL) and RNA binding Fox-1 homologue 3 (RBF3) were seen by immunocytochemistry (Extended Data Fig. 5h) or RT–qPCR (Extended Data Fig. 5i). Minor differences in transcript levels were seen for MAP2, but these changes did not show an interaction between *APOE* and *SORT1* genotypes (Extended Data Fig. 5i).

Fig. 2 | Loss of sortilin or the presence of apoE4 prevents consumption of LCFAs in neuronal mitochondria. Quantification of real-time cellular OCRs in synaptosomes isolated from brain cortices of male mice of the indicated *Sort1* and human *APOE* genotypes (12 weeks of age). OCR was measured under basal conditions (0–20 min) and following sequential addition of oligomycin, FCCP and R/A at the indicated time points. **a**, OCR in synaptosomes of the indicated genotypes cultured for 2 h in media lacking pyruvate, glucose and glutamine, but containing 300 μ M palmitate. Data of three independent experiments are shown. Each data point represents the mean of 12–15 technical replicates. **b–m**, Dependency of mitochondrial respiration in synaptosomes in the indicated genotypes on fatty acid substitution tested as described above. Synaptosomes

were kept in low glucose conditions (1 mM sodium pyruvate, 2 mM glucose, 1 mM glutamine) and either non-treated (control) or pretreated with 300 μ M palmitate (**b–e**), 100 μ M acetic acid or 100 μ M butyric acid (**f–i**) or 200 μ M heptanoic acid or 200 μ M octanoic acid (**j–m**). For each genotype, one exemplary experiment is shown (to the left) as well as the quantification of the percentage of maximal respiration as compared to control treatment of the same genotype (set to 100%). Data are given as the mean \pm s.d. of $n = 3$ biological replicates (animals). Each biological replicate is the mean of $n = 8–15$ technical replicates. Statistical significance was tested using an unpaired Student's *t*-test (two-tailed). Individual respiration profiles of three independent experiments for each condition are given in Supplementary Figs. 4–6.



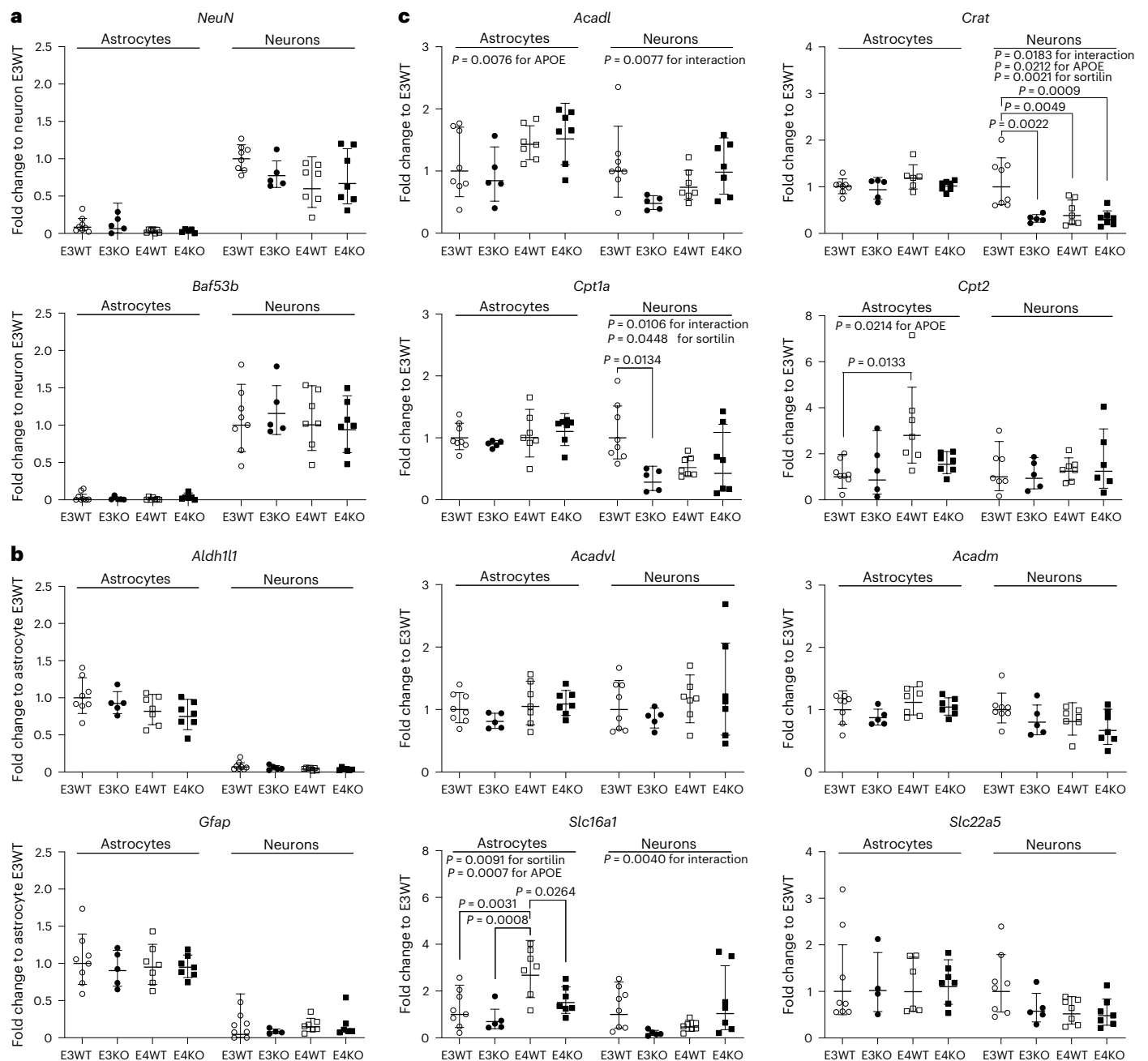


Fig. 3 | Loss of sortilin or the presence of apoE4 impacts metabolic gene expression profiles in mouse neurons but not astrocytes. Gene expression patterns were compared in neurons and astrocytes isolated from the brains of male mice (12 weeks of age) of the indicated *Sort1* and human *APOE* genotypes using fluorescence-activated cell sorting (E3WT $n = 8$, E3KO $n = 5$; E4WT and E4KO $n = 7$ mice). Individual data points and the mean \pm s.d. of the entire genotype group are given. Statistical significance was tested using two-way ANOVA with Tukey's multiple-comparison test. Each cell preparation was performed as an independent experiment. **a, b**, RT-qPCR analyses of neuronal markers *NeuN* and *Baf53b* (**a**) as well as astrocyte-specific markers *Aldh1l1* and

Gfap (**b**) confirm the purity of sorted neuronal and astrocyte cell preparations. **c**, RT-qPCR analyses of genes encoding enzymes in transport and metabolism of fatty acids document interaction of *APOE* and *Sort1* genotypes in neurons but not astrocytes. *Acadl*, acyl-CoA dehydrogenase long chain; *Acadmv*, acyl-CoA dehydrogenase medium chain; *Acadm*, acyl-CoA dehydrogenase very long chain; *Cpt1a*, carnitine *O*-palmitoyltransferase 1A; *Cpt2*, carnitine *O*-palmitoyltransferase 2; *Crat*, carnitine *O*-acyltransferase; *Slc16a1*, solute carrier family 16 member 1 encoding monocarboxylate transporter (MCT) 1; *Slc22a5*, solute carrier family 22 member 5.

Genetic or apoE4-induced sortilin deficiency disrupts lipid fuel choice and synaptic activity in human neurons

To test the consequences of sortilin and apoE3 interaction for energy homeostasis in human neurons, we compared mitochondrial respiration in E3WT, E3KO, E4WT and E4KO iNs supplemented with conditioned medium from iAs of the corresponding *APOE* and *SORT1* genotypes. Maximal respiration was always compared in neuronal cultures untreated

(solvent control) or treated with UK5099 or etomoxir. Mirroring phenotypes seen in mouse synaptosomes, maximal respiration decreased in E3WT iNs when treated with UK5099 or etomoxir in the presence of normal glucose levels (Fig. 4a and Supplementary Fig. 8a). By contrast, maximal respiration in E3KO iNs (Fig. 4b and Supplementary Fig. 8b), E4WT iNs (Fig. 4c and Supplementary Fig. 8c) or E4KO iNs (Fig. 4d and Supplementary Fig. 8d) was reduced by UK5099 but not by etomoxir.

To unequivocally confirm the insensitivity of sortilin-deficient iNs to etomoxir, we used a second independent *APOE* $\epsilon 3/\epsilon 3$ iPS cell line (designated E3*), either WT (E3*WT) or genetically deficient (E3*KO) for *SORT1* (Extended Data Fig. 6a–f). When differentiated to iNs (Extended Data Fig. 6g,h), a robust impact of etomoxir on maximal respiration was seen in E3*WT (Extended Data Fig. 6i and Supplementary Fig. 9a) but not in E3*KO (Extended Data Fig. 6j and Supplementary Fig. 9b) neurons. As with mouse synaptosomes, these metabolic alterations were not due to structural alterations in mitochondria, as mitochondrial area (Extended Data Fig. 7a,b), levels of mitochondrial proteins (Extended Data Fig. 7c) or architecture of mitochondria (Extended Data Fig. 7d,e) did not show genotype interaction.

To test our hypothesis, that sortilin's action in neuronal lipid homeostasis was disrupted by binding of apoE4 to this receptor (see our model in Fig. 1a), we compared the sensitivity of E4WT iNs to etomoxir in the presence of conditioned medium from either E4WT or E3WT iAs. As shown in Fig. 4c, maximal respiration in E4WT iNs was insensitive to etomoxir when neurons were exposed to conditioned medium from E4WT astrocytes (Fig. 4e,g and Supplementary Fig. 10a). However, sensitivity to etomoxir was restored in E4WT iNs when exposed to medium conditioned by E3WT iAs (Fig. 4f,g and Supplementary Fig. 10b).

Jointly, our findings in mouse and human cell models corroborated our hypothesis that genetic (E3KO, E4KO) or functional (E4WT) deficiency of sortilin disrupts the ability of neurons to support mitochondrial energy homeostasis through LCFA consumption. To query the impact of altered metabolic fuel choice on neuronal activity, we compared electrical activities in E3WT and E3KO iNs using multielectrode arrays (MEAs). Because neurons require physical contact with astrocytes for synaptic maturation on MEA plates, we followed established protocols co-culturing human E3WT and E3KO iNs with primary mouse astrocytes from E3WT and E3KO mice, respectively²⁸. When fully supplemented with glucose, electrical activities, including burst duration, burst count and network burst count, were comparable in both genotypes (Fig. 4h and Extended Data Fig. 8a,b). These findings documented that sortilin deficiency per se did not impact synapse function in our model. To explore the impact of fuel choice on electrical activity, we next assayed mature E3WT and E3KO iNs in glucose-deficient media in the absence or presence of palmitate. Burst duration, burst count and network burst count all significantly deteriorated in E3WT iN cultures when treated with media lacking glucose and palmitate (Fig. 4i–k). Neuronal activities also decreased in glucose-deficient media supplemented with palmitate, but this decrease was not statistically significant when compared to media containing full glucose

and palmitate (pre-condition; Fig. 4i–k and Extended Data Fig. 8c). By contrast, electrical activities significantly decreased in E3KO iNs in the absence of glucose, regardless of the absence or presence of palmitate (Fig. 4i–k and Extended Data Fig. 8d).

***SORT1* deficiency decreases the levels of PUFAs and eCBs in human apoE3 neurons**

We previously reported that levels of PUFAs and endocannabinoids (eCBs) were decreased in the brains of E3KO, E4WT and E4KO mice as compared to E3WT animals¹⁴. We suggested that this defect may reflect the inability of sortilin-deficient neurons to take up apoE-bound PUFAs and to convert them into eCBs, neuroprotective signalling mediators produced in neurons on demand²⁹.

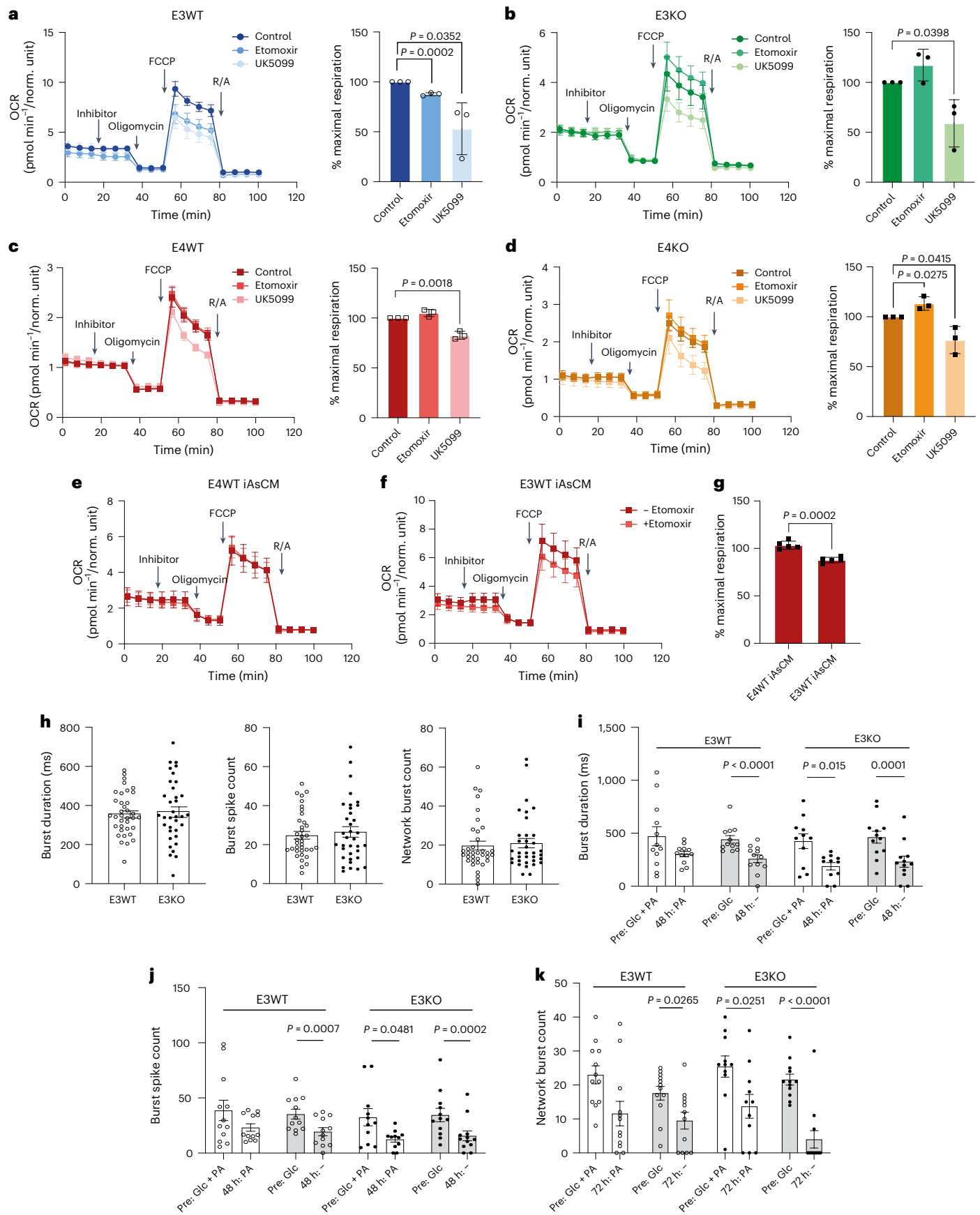
To substantiate our hypothesis and its relevance for neuroprotective actions of eCBs in the human brain, we performed lipidomics analyses in our iPS cell-derived cell models. In detail, we cultured iNs of defined *SORT1* and *APOE* genotypes for 10 days in conditioned medium from iAs of the same genotypes and measured neuronal lipid levels by LC–MS/MS thereafter. Loss of sortilin in E3KO iNs resulted in a drastic decrease in cellular content of PUFAs when compared with the isogenic E3WT line (Fig. 5a). Among other lipids, levels of $\omega 6$ and $\omega 3$ PUFAs were reduced, as well as levels of the eCB precursors linoleic acid (C18:2n-6) and docosahexaenoic acid. Sortilin deficiency also decreased neuronal levels of several eCBs and eCB-like metabolites, including 2-arachidonoylglycerol, synaptamide and linoleoyl ethanolamide, and caused a concomitant increase in levels of anandamide (Fig. 5a). Depletion of PUFA and eCB contents in E3KO neurons was not due to alterations in levels of these lipids released by iAs as the concentrations of the tested lipids were comparable in conditioned media from E3WT and E3KO iAs (Fig. 5b). Importantly, *SORT1* deficiency did not alter the concentrations of most PUFAs and eCBs in E4KO iNs when compared with isogenic E4WT neurons (Extended Data Fig. 9), a finding in agreement with apoE4 rendering WT neurons functionally deficient for sortilin.

Loss of sortilin or the presence of apoE4 impairs PPAR-dependent gene expression in human neurons

eCBs and eCB-like metabolites exert their cellular functions through various molecular mechanisms, including by acting as ligands for transcription factors of the PPAR gene family^{30,31}. To query the consequence of decreased PUFA and eCB levels in E3KO iNs, we performed comparative expression profiling of PPAR target genes in E3WT and E3KO iNs. Using a microarray-based strategy to assess transcript levels of

Fig. 4 | Loss of sortilin or the presence of apoE4 causes metabolic and functional defects in human neurons. a–d, Quantification of real-time cellular OCR in induced human neurons: E3WT (a), E3KO (b), E4WT (c) or E4KO (d). Neurons were cultured in the presence of medium conditioned by astrocytes of the same genotypes. OCR was measured under basal conditions (0–20 min) and following sequential addition of oligomycin, FCCP and R/A. In addition, neurons were treated with solvent control buffer or solutions containing 8 μ M UK5099 or 16 μ M etomoxir at the indicated time points (inhibitor). OCR measurements were normalized (norm.) to the cell count (per 1,000 cells) in each well, determined after completion of the assay using Hoechst dye (see Methods for details). For each genotype, one exemplary experiment is shown as well as the quantification of the percentage of maximal OCR as compared to the control buffer treatment of the same genotype for the entire dataset (set to 100%). Data represent the mean \pm s.d. of $n = 3$ biological replicates. Each biological replicate is the mean of $n = 10$ –15 technical replicates. Statistical significance was tested using an unpaired Student's *t*-test (two-tailed). Individual respiration profiles for all three experiments are given in Supplementary Fig. 8. **e,f**, Induced human E4WT neurons were cultured in the presence of media conditioned by E4WT astrocytes (E4WT iAsCM; e) or E3WT astrocytes (E3WT iAsCM; f) for 8 days. Subsequently, real-time cellular OCR was determined in the absence (–) or presence (+) of 16 μ M etomoxir (inhibitor). One exemplary respiration profile for each condition is shown. Each data point represents the mean of 20–23 technical replicates.

Individual respiration profiles for all five independent experiments are given in Supplementary Fig. 10. **g**, Maximal OCR determined in experimental conditions shown in e and f documents rescue of sensitivity to etomoxir in E4WT neurons when treated with conditioned media from E3WT (E3WT iAsCM) but not from E4WT (E4WT iAsCM) astrocytes. Statistical significance was tested using an unpaired Student's *t*-test (two-tailed). **h**, MEA analysis of burst duration, burst spike count and network burst count in E3WT and E3KO iNs, cultured in 25 mM glucose, 0.23 mM sodium pyruvate and 2 mM glutamine (days 31–38 of culture). Individual biological replicates ($n = 36$ for E3WT, $n = 35$ for E3KO) of three individual differentiation experiments are shown. Individual data points and the mean \pm s.e.m. for each genotype group are presented. Statistical significance was tested using an unpaired Student's *t*-test (two-tailed). **i–k**, MEA analysis of burst duration (i), burst spike count (j) and network burst count (k) in E3WT and E3KO iNs (days 37–38 of culture) cultured in media without glucose or pyruvate, in the presence (PA) or absence (–) of 100 μ M palmitate for 48–72 h. Neuronal activity in each well was compared to the pretreatment condition (25 mM glucose, 0.23 mM sodium pyruvate, 2 mM glutamine) with or without palmitate for 6 h. Individual biological replicates ($n = 12$; $n = 11$ for E3KO (PA)) of two individual differentiation experiments are given. Data are presented as the mean \pm s.e.m. with individual data points. Statistical significance was determined using a paired Student's *t*-test (two-tailed).



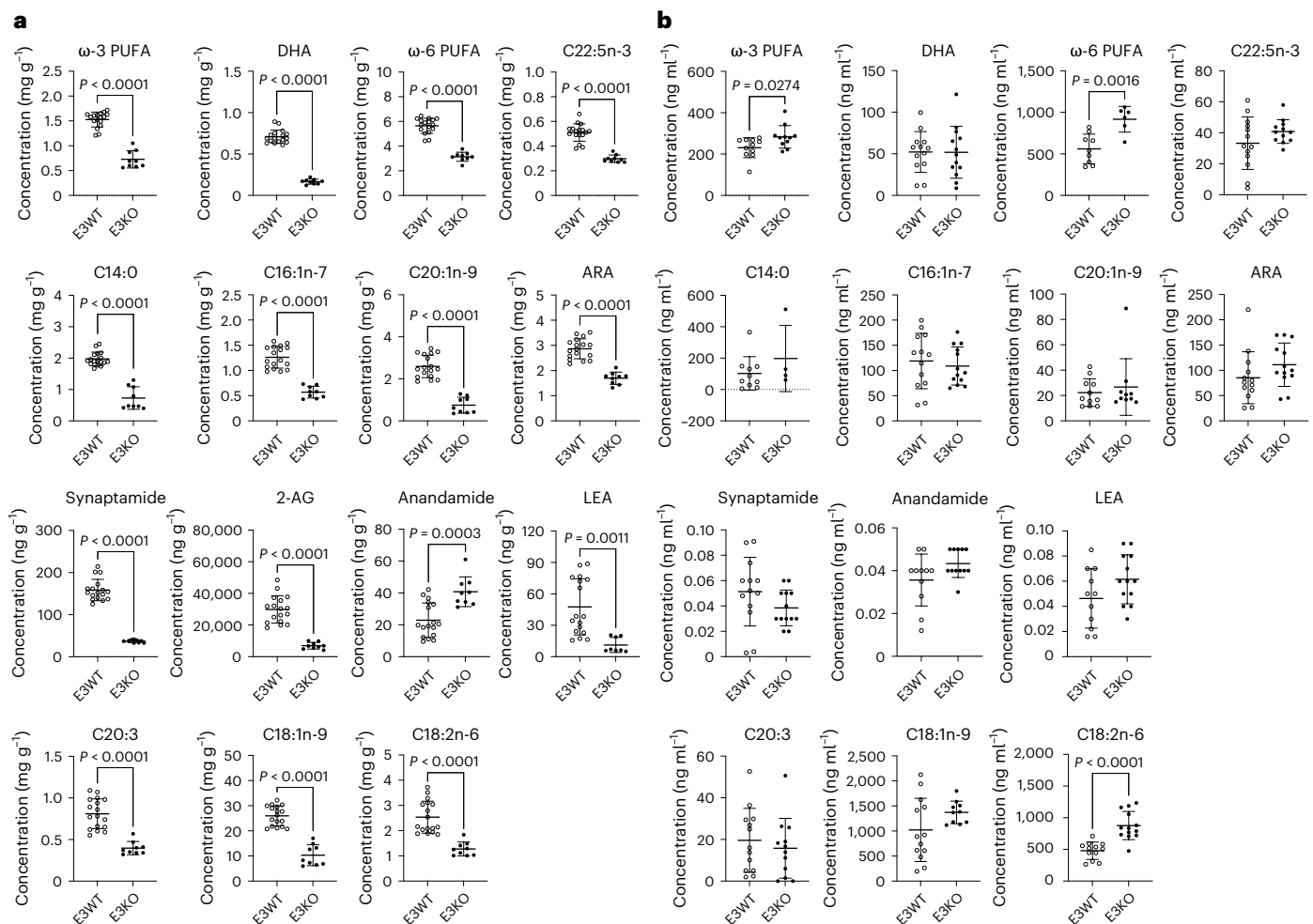


Fig. 5 | *SORT1* deficiency decreases the levels of PUFAs and eCBs in human E3 neurons. a, Concentrations of selected lipids in iPS cell-derived cortical neurons were determined using LC-MS/MS. Neurons (day 12 of culture) were *APOE* $\epsilon 3/\epsilon 3$ and either WT (E3WT) or genetically deficient for *SORT1* (E3KO). Individual biological replicates ($n = 17$ for E3WT, $n = 9$ for E3KO) of 2–3 individual differentiation experiments are given. **b**, Concentrations of selected lipids in the cell supernatant of iPS cell-derived E3WT and E3KO astrocytes (days 21–28 of

culture) were determined using LC-MS. Individual biological replicates ($n = 4–13$, depending on the analysed lipid) of 4–6 individual differentiation experiments are shown. Individual data points and the mean \pm s.d. of the entire genotype group are shown. Statistical significance was tested using an unpaired Student's *t*-test (two-tailed). ARA, arachidonic acid; 2-AG, 2-arachidonoylglycerol; DHA, docosahexaenoic acid; LEA, linoleoyl ethanolamide.

84 PPAR targets, we identified 30 transcripts that were dysregulated in E3KO compared to isogenic E3WT iNs (Fig. 6a,b). Most of these genes showed reduced transcript levels when neurons lacked the receptor (Fig. 6c). With relevance to lipid homeostasis, decreased transcript levels included those encoding *ACADL*, carnitine transporter *SLC22A5*, as well as fatty acid transport proteins *SLC27A1*, *SLC27A5* and *SLC27A6*. Sortilin deficiency also decreased transcript levels of *PPARA* (encoding PPAR α), a master transcriptional regulator of cellular lipid metabolism¹⁹ (Fig. 6d). No impact on transcription was seen for genes encoding PPAR family members PPAR δ and PPAR γ (Fig. 6d). Importantly, no effect of sortilin deficiency on any of the above genes was seen comparing transcription profiles in E4KO and E4WT iNs, corroborating functional sortilin deficiency in the presence of apoE4 (Extended Data Fig. 10).

One transcriptional target of PPAR α with obvious relevance to mitochondrial LCFA consumption was *CPT1A*. Levels of *CPT1A* transcript (Fig. 6e) and *CPT1A* protein (Fig. 6f,g) were significantly higher in E3WT as compared to E3KO, E4WT or E4KO iNs, with no statistically significant difference between the latter three genotypes. Loss of PPAR α -induced expression of *CPT1A* provided a possible molecular explanation for the insensitivity of E3KO or E4 neurons to etomoxir. Alterations in fatty acid handling in neurons lacking sortilin were

also substantiated when testing expression of fatty acid binding proteins (FABPs) in E3WT and E3KO iNs. Loss of sortilin coincided with reduced levels of FABP7, a known sortilin interactor¹⁵ and intracellular carrier for PUFAs and eCBs (Fig. 6h), and with a concomitant compensatory increase in levels of FABP6, an alternative intracellular fatty acid carrier³² (Fig. 6i).

Impaired LCFA fuel use in sortilin-deficient neurons is rescued by induction of PPAR α activity

To ultimately confirm that loss of lipid-induced transcriptional activity of PPAR α contributes to the inability to metabolize LCFAs, we treated E3KO iNs with the PPAR α agonist bezafibrate³³. As expected, induction of PPAR α activity by bezafibrate increased transcript levels of its targets *PPARA* and *CPT1A* in E3KO iNs (Fig. 7a). Importantly, bezafibrate treatment also conferred sensitivity to etomoxir in E3KO iNs as documented by a bezafibrate-induced decrease in maximal respiration in cells treated with etomoxir as compared to control iNs treated with etomoxir in the absence of bezafibrate (Fig. 7b,c and Supplementary Fig. 11). Similarly to the situation in E3KO, bezafibrate treatment also increased PPAR α activity in E4WT and E4KO iNs (Fig. 7d,g) and established sensitivity to etomoxir (Fig. 7e,f,h,i and Supplementary Figs. 12 and 13).

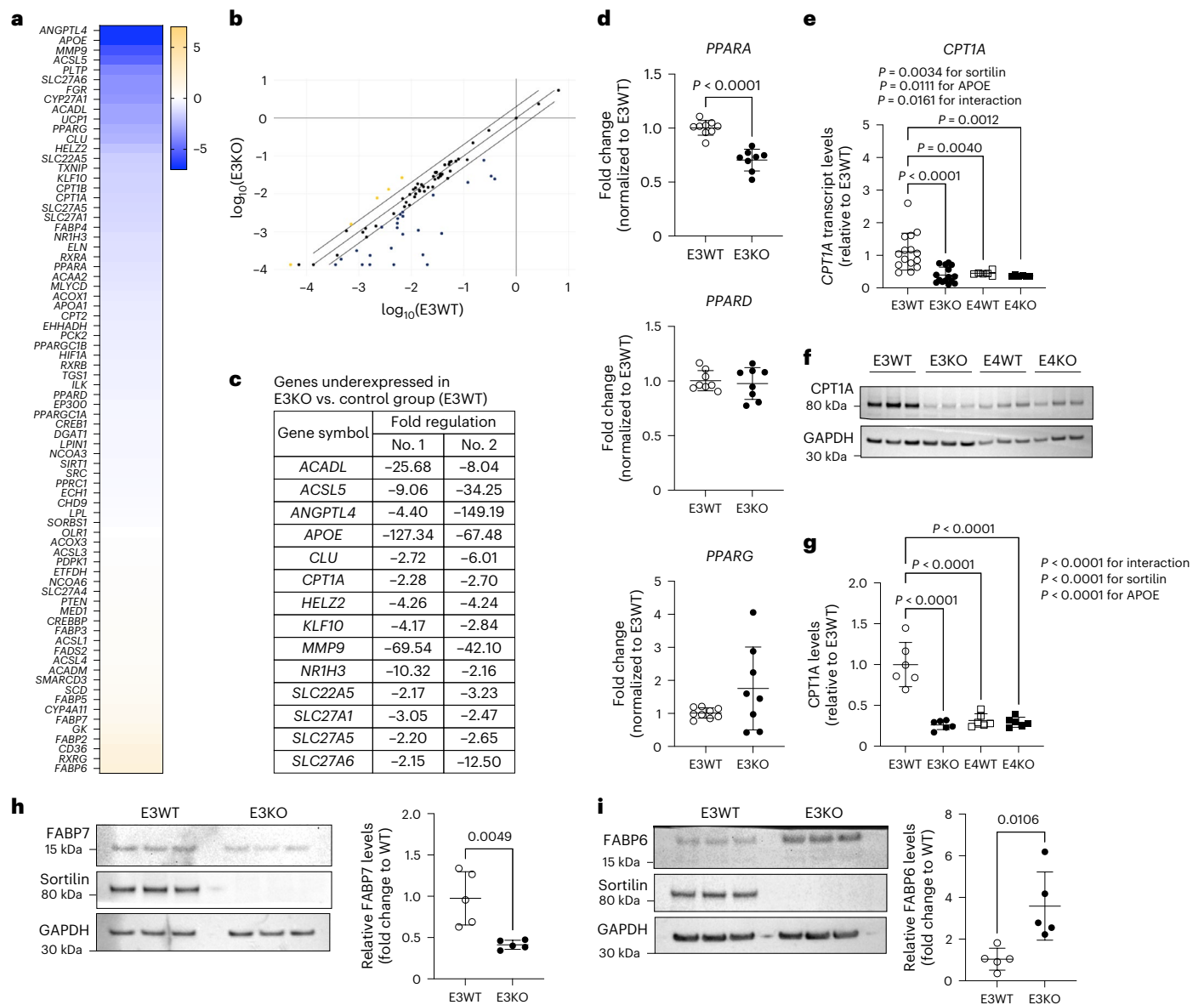


Fig. 6 | Sortilin deficiency disrupts PPAR-dependent gene transcription and expression of fatty acid binding protein 7 in apoE3 iNs. **a–c**, Expression levels of PPAR target genes in iPS cell-derived neurons treated with iPS cell-derived astrocyte-conditioned media were tested using the Human PPAR Targets RT² Profiler PCR Array. Neurons (day 12 of culture) were *APOE* $\epsilon 3/\epsilon 3$ and either WT (E3WT) or genetically deficient for *SORT1* (E3KO). One exemplary experiment from a total of $n = 2$ individual biological replicates is shown. **a**, Expression levels are given as a heat map with levels in E3KO presented as \log_2 fold change compared to E3WT (set to 0). The blue and yellow spectra indicate downregulated and upregulated genes, respectively. **b**, Scatterplot analysis comparing \log -transformed relative expression for all tested PPAR target genes in E3WT and E3KO neurons. The central diagonal line indicates unchanged gene expression, while the outer diagonal lines indicate the 2-fold regulation threshold. Genes with >2 -fold differences in transcript level between groups are presented as blue and yellow dots, indicating downregulated or upregulated genes, respectively. **c**, Selected list of genes downregulated by >2 fold in E3KO compared to E3WT neurons. Data from two independent experiments are shown. **d**, RT-qPCR analysis of the indicated genes in E3WT and E3KO human neurons treated with iAsCM (day 12 of culture). Individual biological replicates ($n = 8–9$, depending on the analysed gene) of two individual differentiation experiments, as well as mean \pm s.d. of the entire genotype group, are shown. Data were normalized to GAPDH and expressed as relative to the E3WT group from the same

differentiation experiment. Statistical significance was tested using an unpaired Student's *t*-test (two-tailed). **e**, *CPT1A* transcript levels in human neurons of the indicated *SORT1* and *APOE* genotypes treated with iAsCM were tested using RT-qPCR. Individual data points ($n = 15$ for E3WT and E3KO, $n = 6$ for E4WT and E4KO) from 2–4 individual differentiation experiments, as well as mean \pm s.d. of the entire genotype group, are shown. Statistical significance was tested using two-way ANOVA with Tukey's multiple-comparison test. **f, g**, Levels of *CPT1A* protein were determined in total lysates of human neurons (day 12 of culture) of the indicated *SORT1* and *APOE* genotypes treated with iAsCM using western blotting (**f**) and densitometric scanning of replicate blots thereof (**g**). Detection of GAPDH served as the loading control. Data in **g** represent data points from individual biological replicates ($n = 6$) of 2–3 individual differentiation experiments. Individual data points and the mean \pm s.d. of the entire genotype group are shown and given as relative to E3WT (set to 1). Statistical significance was tested using two-way ANOVA with Tukey's multiple-comparison test. **h, i**, Levels of FABP7 (**h**) and FABP6 (**i**) as determined by western blotting in total lysates from human neurons of the indicated *SORT1* and *APOE* genotypes. For each panel, one exemplary western blot and quantitative analysis from densitometric scanning of replicate blots (normalized to GAPDH) are shown. Values represent the mean \pm s.d. of $n = 5$ biological replicates (from two individual differentiation experiments). Statistical significance was tested using an unpaired Student's *t*-test (two-tailed).

Of note, the ability of bezafibrate to promote LCFA consumption in cells lacking the endocytic receptor sortilin argued that these experimental conditions reflect the consumption of intracellular lipid stores.

In conclusion, our data identified a new concept in neuronal energy homeostasis and the central role of the apoE receptor sortilin in this process (Fig. 7j). We propose that endocytic uptake of lipidated apoE3 by this receptor delivers PUFAs to neurons to be converted into ligands for the transcriptional activator PPAR α . As shown in established cell lines before, apoE3 uptake also requires the interaction of sortilin with the carrier FABP7, facilitating intraneuronal lipid transport¹⁵. PPAR α -dependent induction of metabolic gene expression enables neurons to use LCFAs as metabolic fuel under basal as well as under glucose-restricted conditions. This pathway is lost in the presence of apoE4 that disrupts sortilin's endocytic ability, resulting in impaired PUFA uptake and loss of PPAR α activation. Ultimately, neurons exposed to apoE4-containing lipoproteins are unable to efficiently utilize LCFAs as metabolic fuel. Instead, they revert to PPAR α -independent mitochondrial import of medium-chain and short-chain fatty acids, energetically less favourable substrates to support energy production.

Discussion

Healthy neurons largely rely on glucose for energy production, contributing to a substantial portion of the metabolites consumed by the human body. However, availability of glucose becomes limited during various stress conditions, such as brain ageing^{34–39}. Reduced metabolism of glucose is also a feature of the brain in Alzheimer disease^{40–42} and FTD^{43,44}, aggravating the deterioration of neuronal functions. Limited availability of glucose enforces a switch in neurons to alternative metabolic fuels, including ketone bodies⁴⁵ and fatty acids⁴⁶. Lipids as metabolic fuel came into recent focus with studies showing that the inability of neurons to mobilize fatty acids from triglycerides, due to neuron-specific triglyceride lipase deficiency, results in respiratory dysfunction and a decrease in ATP production, albeit at normal glucose metabolism^{47,48}.

The use of LCFAs as neuronal fuel under basal as well as glucose-restricted conditions is also documented by findings in this study. As shown in substrate oxidation stress tests, blockade of mitochondrial import of LCFAs by etomoxir decreases maximal respiration in E3WT mitochondria, even in the presence of sufficient glucose supply. This effect is seen in mouse synaptosomes (Fig. 1g) and human neurons (Fig. 4a). These findings argue that LCFA consumption helps to raise neuronal energy production to meet maximal demand, even if sufficient glucose is available. Induced expression of genes related to LCFA consumption in neurons sorted from E3WT mouse brains, as

compared to E3KO and E4 neurons (Fig. 3), further substantiate the relevance of this pathway for in vivo brain lipid metabolism under normal (that is, full glucose) conditions.

The demand for lipid fuel becomes heightened in situations of limited glucose supply, as shown by mitochondrial stress tests performed with 20% of normal glucose levels. Under these conditions, E3WT mitochondria are able to use LCFAs to increase neuronal energy production (Fig. 2b), an ability blunted in E3KO and E4 mitochondria (Fig. 2c–e). Finally, in situations of glucose depletion, respiration is maintained in E3WT, but completely shut down in E3KO and E4 synaptosomes (Fig. 2a). Along these lines, electrical activity is comparable in E3WT and E3KO neurons fully supplemented with glucose (Fig. 4h). Following glucose depletion, E3WT neurons can use LCFA consumption to sustain electrical activity, an ability absent in sortilin-deficient cells (Fig. 4i–k).

Taken together, our findings support a model whereby LCFAs help to increase neuronal energy production to meet maximal demand under basal glucose conditions, and that this fuel becomes essential for vital neuronal functions as supply with glucose decreases. As purified synaptosomes lack the ability to acutely induce gene expression in response to changing experimental conditions, their ability to consume fatty acids of various chain lengths in mitochondrial stress tests is defined by the enzyme repertoire expressed in the mouse brain at the time of sample preparation. Accordingly, neurons in the E3WT brain express enzymes to metabolize LCFAs (and MCFAs) but not SCFAs, a less favoured lipid fuel. The converse situation holds true for E3KO and E4 neurons, reflecting a switch to the use of SCFAs that is already inherent to the brain of these animals in vivo. Of course, these data do not dispute the ability of E3WT neurons to transcriptionally induce pathways to consume SCFAs, if required to do so. Similarly to males, synaptosomes prepared from female mice also show an interaction of apoE and sortilin genotypes in defining sensitivity to etomoxir (Extended Data Fig. 2). Although these data do not allow us to conclude that neuronal mitochondria from female mice are indistinguishable from male samples in every aspect tested in this study, we currently have no evidence to suggest gender-specific differences in sortilin and apoE interaction in neuronal energy homeostasis.

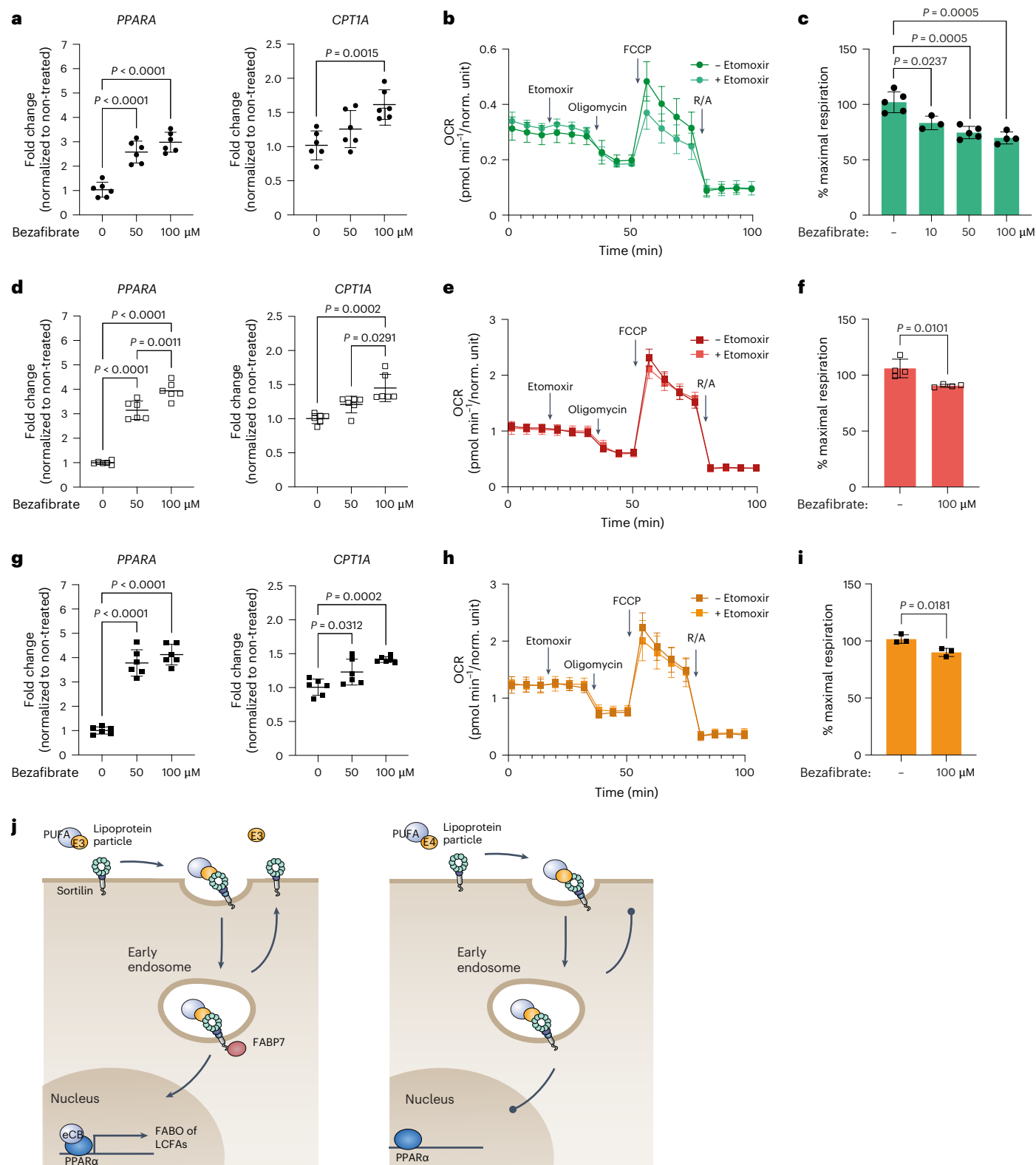
Recent findings document metabolic distinctions between mitochondria in neuronal soma versus axonal endings⁴⁹, a question not addressed in our study. As food for thought, we see comparable mitochondrial phenotypes in mouse synaptosomes (that is, synaptic mitochondria) and in induced human neurons (mainly somatic mitochondria). Although comparing mitochondria from human and mouse models, our findings suggest that the need for LCFAs as metabolic fuel is a feature seen in mitochondria in soma and axonal endings.

Fig. 7 | Rescued use of LCFAs as metabolic fuel in human E3KO and E4 neurons by PPAR α agonist bezafibrate. a, Transcript levels of *CPT1A* and *PPARA* in human E3KO neurons were tested using RT–qPCR. Cells have not been treated (0) or pretreated with the indicated concentrations of bezafibrate. Individual data points from $n = 6$ biological replicates (three individual differentiation experiments) and the mean \pm s.d. of the entire genotype group are shown. Statistical significance was tested using one-way ANOVA with Bonferroni's multiple-comparisons test. b, c, The dependency of mitochondrial respiration on PPAR α activity was assessed by pretreatment of human E3KO iNs with bezafibrate for 48 h before substrate oxidation stress test in the presence of solvent control buffer or a solution containing 16 μ M etomoxir. OCR measurements were normalized (norm.) to the cell count (per 1,000 cells) in each well, determined after completion of the assay using Hoechst dye (see Methods for details). One exemplary experiment using 100 μ M bezafibrate in the presence or absence of etomoxir is shown (b) as well as the quantification of the percentage of maximal respiration as the mean \pm s.d. from $n = 3$ biological replicates ($n = 10–15$ technical replicates) of etomoxir-treated versus non-etomoxir-treated E3KO neurons in the absence or presence of the indicated concentrations of bezafibrate (c). Statistical significance of data in c was tested using an unpaired Student's t -test (two-tailed). Individual respiration profiles for 3–5 experiments per condition are given in

Supplementary Fig. 11. d–i, The dependency of mitochondrial respiration on PPAR α activity was assessed by pretreatment of human E4WT (d–f) or E4KO (g–i) neurons with 100 μ M bezafibrate for 48 h. Panels d and g document *CPT1A* and *PPARA* transcript levels as tested in a above. Individual data points from $n = 6$ biological replicates (three individual differentiation experiments) and the mean \pm s.d. of the entire genotype group are shown. Panels e, f, h and i depict substrate oxidation stress tests in the presence of solvent control buffer or a solution containing 16 μ M etomoxir (as detailed in b and c). One exemplary experiment using 100 μ M bezafibrate in the presence or absence of etomoxir is given (e and h) as well as the quantification of the percentage of maximal respiration as the mean \pm s.d. from $n = 3$ biological replicates ($n = 8–12$ technical replicates) of etomoxir-treated versus non-etomoxir-treated E4 neurons in the absence or presence of bezafibrate (f and i). Statistical significance was tested using an unpaired Student's t -test (two-tailed). Individual respiration profiles for four experiments per condition for E4WT and three experiments per condition for E4KO are given in Supplementary Figs. 12 (E4WT) and 13 (E4KO). j, Model of sortilin and apoE isoform-specific interaction in facilitation of PPAR α -dependent mitochondrial respiration of LCFAs. This pathway is operable with apoE3 (left schematic) but lost with apoE4 (right schematic). E, apoE; FABO, fatty acid beta oxidation.

What may be the molecular pathway whereby sortilin determines alternative metabolic fuel choices in neurons? Using targeted lipidomics, we show that loss of sortilin activity in human E3KO neurons coincides with a drastic reduction in neuronal levels of PUFAs and their bioactive derivatives, most notably eCBs and eCB-like metabolites (Fig. 5a). These findings recapitulate data shown by us in mouse brains before¹⁴. Loss of PUFAs is attributed to a prominent role of the receptor in neuronal uptake of lipidated apoE, providing essential lipids for

cellular lipid metabolism and action^{10,14}. Several apoE receptors have been documented in neurons, including the low-density lipoprotein receptor, the low-density lipoprotein receptor-related protein 1 and the apoE receptor 2 (reviewed in ref. 12). Loss of sortilin activity in gene-targeted mice increases circulating levels of apoE in the brain, due to impaired cellular clearance of the carrier¹⁰. Sortilin deficiency also reduces apoE uptake in primary mouse neurons by approximately 70%¹⁰. Such pronounced clearance defects have not been reported



in other apoE receptor-deficient models. As well as by quantity, sortilin may also distinguish itself from other apoE receptors by functionality as it interacts with FABP7 (ref. 15). FABP7 is a brain-specific lipid chaperone for cytosolic trafficking of PUFAs and eCBs^{50–52}. FABP7-dependent trafficking is required for biosynthesis of eCBs from PUFAs, and for their delivery to nuclear PPARs for regulation of gene transcription^{53–56}. Sortilin is essential for proper sorting and stable expression of FABP7 in established cell lines¹⁵, a mechanism now supported by data in human neurons (Fig. 6h). Thus, sortilin is in a unique position among the various apoE receptors to link extracellular (that is, apoE) and intracellular (that is, FABP7) PUFA transport processes in neurons.

Given the drastic decrease in PUFA and eCB levels in E3KO iNs as compared to isogenic E3WT cells, impaired activation of PPAR α is a likely reason for alterations in mitochondrial lipid handling in this genotype. This conclusion is supported by decreased levels of synaptamide, 2-arachidonoylglycerol and linoleoyl ethanolamide (Fig. 5a), known ligands of this transcription factor^{57,58}. Impaired activity of PPAR α in human neurons lacking sortilin is substantiated by the reduced expression of multiple transcriptional targets with relevance to lipid handling, most notably CPT1A, the mitochondrial importer for LCFA (Fig. 6a–g). Importantly, the insensitivity to etomoxir seen in E3KO and E4 iNs can be rescued by bezafibrate, supporting impaired PPAR α activity as the likely molecular cause of the mitochondrial import defect for LCFAs (Fig. 7a–i). Conceivably, absent transcriptional activation of PPAR α targets other than CPT1a may contribute to metabolic imbalance in sortilin-deficient neurons, a possibility that warrants further investigation.

The metabolism of neurons is intimately linked to that of astrocytes which support neurons with apoE-bound lipids and other metabolites. Recent studies have documented dysregulation in astrocyte metabolism^{59–62} and lipid homeostasis^{63,64} in response to ageing or apoE4. This conclusion is also supported by apoE genotype-dependent changes in transcriptional profiles in primary E3 versus E4 astrocytes seen in this study (Fig. 3). Also, prior work reported differences in lipid-loading comparing apoE variants^{65,66}. Our studies do not exclude that differences in lipid composition may contribute to distinct metabolic and functional phenotypes seen in neurons exposed to apoE3-containing versus apoE4-containing lipoproteins. However, LCFA, PUFA and eCB precursors showed comparable levels in media conditioned by apoE3 (Fig. 5b) or apoE4 (Extended Data Fig. 9b) expressing WT astrocytes. These findings support our concept that impaired neuronal uptake and conversion, rather than reduced exogenous availability of fatty acids, causes major metabolic phenotypes seen in E3KO and in E4 neurons herein. PUFAs and eCBs have numerous functions in cell metabolism and action. Thus, reduced fatty acid levels in neurons lacking sortilin possibly impact multiple cellular activities related to lipid homeostasis, or even unrelated receptor actions^{1,67,68}. Still, the ability of bezafibrate to rescue the sensitivity of E3KO and E4 iNs to etomoxir argues that induction of LCFA import through CPT1A expression, among other metabolically relevant targets of PPAR α , explains the metabolic phenotypes distinguishing sortilin-expressing from sortilin-deficient neurons.

SORT1 shows genome-wide association both with Alzheimer disease¹⁷ and FTD¹⁸, the two most common forms of age-related dementias in patients. This association argues for a crucial function of the receptor in healthy ageing of the brain. Sortilin's role in FTD is linked to its ability to act as clearance receptor for progranulin, a major aetiological agent in FTD^{69–71}, while its mode of action in Alzheimer disease remains unclear. As both dementias are characterized by a hypometabolism of glucose^{40–44,72}, deteriorating lipoprotein receptor functions of sortilin in the ageing brain may well aggravate deficits in neuronal energy production in the older population.

An additional mechanism specific to Alzheimer disease concerns the detrimental impact of apoE4 on sortilin activity. Similarly to other

receptors bound by apoE^{73,74}, binding of apoE4 traps internalized sortilin in early endosome, preventing discharge of cargo and recycling to the cell surface¹⁵. This noxious propensity of apoE4 is due to an increase in the isoelectric point, as compared to apoE3, resulting in unfolding of the protein in the acidic milieu of endosomes^{75–79}. In our studies, phenotypes in E4WT were indistinguishable from those of E3KO, including alterations in mitochondrial malfunction and in PPAR α deficiency. These findings argue for loss of sortilin activity in the brain of *APOE* ϵ 4 carriers, an assumption corroborated by rescue of sensitivity to etomoxir in E4WT iNs when exposed to apoE3-containing rather than apoE4-containing astrocyte media (Fig. 4e–g). Multiple pathological mechanisms have been reported for apoE4 (reviewed in refs. 80–82). Functional inactivation of sortilin adds another mechanistic explanation to the detrimental actions of this most important genetic risk factor for sporadic Alzheimer disease.

Methods

Mouse models

The generation of mouse strains carrying a targeted replacement of the mouse *ApoE* locus with human *APOE* ϵ 3 or *APOE* ϵ 4 (ref. 20) and being WT (*Sort1*^{+/+}) or genetically deficient for *Sort1* (*Sort1*^{-/-})⁸³ has been described¹⁴. Animals were housed in a controlled environment (12-h light–dark cycle) with access to food and water ad libitum. They were fed a normal mouse chow (4.5% crude fat, 39% carbohydrates). All animal experimentation was conducted in male mice, unless specified otherwise, on an inbred C57BL/6J background following approval by local ethics committees (X9017/17). Animals were 12 weeks of age.

Generation and culture of gene-targeted iPS cell lines

Human iPS cell lines *APOE* ϵ 3/ ϵ 3 (E3WT: <https://hpscereg.eu/cell-line/BIHi005-A/>, male donor; E3*WT: <https://hpscereg.eu/cell-line/BIHi043-A/>, female donor) or *APOE* ϵ 4/ ϵ 4 (E4WT: <https://hpscereg.eu/cell-line/WTSli009-A/>, female donor) were obtained from the MDC Technology Platform Pluripotent Stem Cells (in-house) or the Welcome Trust Sanger Institute. Stem cells were cultured under feeder-free conditions on Matrigel-coated plates (Corning) using Essential 8 Flex medium (Gibco). Cells were passaged using 0.5 mM EDTA solution when the culture reached 80% confluency. To obtain single-cell suspensions, the cells were treated with StemPro Accutase (Gibco) and replated in medium supplemented with 10 μ M of Rock inhibitor (Y27632, Cayman Chemical) for the first 24 h. Cell lines were regularly tested negative for *Mycoplasma*.

To generate sortilin-deficient isogenic subclones of BIHi005-A (designated E3KO), the *SORT1* gene was targeted using transcription activator-like effector nucleases (TALENs) essentially as described⁸⁴. In brief, TALEN constructs were designed to target the *SORT1* start codon using the TALEN Targeter webtool (Cornell University, <https://tale-nt.cac.cornell.edu/node/add/talen/>). Four TALEN segments were digested from an 832-plasmid library (Addgene) using BsmBI and ligated into a TALEN vector carrying a FokI endonuclease domain, and either GFP or RFP (*SORT1* ATG left-GFP: I: CGGC, II: GGCA, III: TTCC, IV: GCG; *SORT1* ATG right-RFP: I: CCGC, II: AGCT, III: CCCC IV: AGG). TALEN pairs were transfected into BIHi005-A iPS cells using Lipofectamine 3000 (Thermo Fisher) according to the manufacturer's instructions. Cells were subjected to fluorescence-activated cell sorting 48 h after transfection based on GFP and RFP expression. The double-positive cells were replated at low density in Essential 8 medium to form single-cell colonies. Colonies were expanded and genomic DNA extracted for PCR amplification of the ATG region of *SORT1* (forward primer: 5'-CGTCCAGCCAATCAGTCCC-3'; reverse primer: 5'-AGCTTGCGCAGCAAGTCC-3'). PCR products were analysed on 2% agarose gels to identify insertions or deletions, followed by Sanger sequencing to verify a homozygous disruption of the ATG. Positive clones were quality controlled for karyotype stability and cryopreserved.

To generate sortilin-deficient isogenic subclones of HPSI0913i-diku_1 cells (named E4KO), we utilized the CRISPR–Cas9 genome-editing system as described in STAR protocols⁸⁵. In brief, a single guide RNA targeting exon 4 of *SORT1* was designed using the Synthego knockout guide design tool (<https://design.synthego.com/>). The single guide RNA sequence (5'-GCCAAATTCAGTCCGAATAA-3') obtained from Integrated DNA Technologies (<https://eu.idtdna.com/>) and complexed with Hi.Fi Cas9 to form ribonucleoprotein particles, which were transfected into HPSI0913i-diku_1 cells using the Neon transfection 10 µl kit (Thermo Fisher Scientific), according to the manufacturer's instructions. Editing efficiency was estimated 48 h after transfection by Sanger sequencing, and data were analysed using the Synthego ICE tool. To isolate single-cell clones, we used the automated Iota Sciences IsoCell platform. Targeted clones were identified by Sanger sequencing and inference of CRISPR edit analysis, quality controlled for karyotype stability and tested regularly as negative for *Mycoplasma*.

A sortilin-deficient clone of *APOE*ε3/ε3 iPS cell line HMGU001-A/BiHi043-A, designated E3*KO (<https://hpscereg.eu/cell-line/BiHi268-A-31/>), was generated as described for E4KO above.

Bioenergetic assays in synaptosomes

Mice were euthanized by cervical dislocation and the brain cortices dissected on ice. The cortices were manually homogenized in gradient buffer (0.32 M sucrose, 5 mM Tris-HCl, 5 mM EDTA, 0.25 mM dithiothreitol) using a glass Dounce homogenizer (Bellco Glass, 1984-10002). Nuclear material was removed by centrifugation at 1,000g for 10 min at 4 °C. The supernatant was applied onto a Percoll density gradient with 23%, 10% and 3% Percoll in gradient buffer. The gradient was centrifuged at 29,000g for 15 min at 4 °C using a Sorvall SS-34 rotor. The gradient fraction at the interface between the 23% and 10% Percoll containing synaptosomes were collected and protein concentration determined by Pierce Bradford Protein Assay Kit (Thermo Fisher Scientific, 23200).

Twenty micrograms of synaptosomal protein in a volume of 80 µl was added to each well of a Seahorse XFe96/XF Pro Cell Culture Microplate (Agilent Technologies, 103792-100) coated with polyethylenimine (Sigma-Aldrich, P3143). The mitochondria-loaded XF microplate was centrifuged at 1,900g for 20 min at 4 °C for adherence of the synaptosomes. Pre-warmed assay media (2 mM MgSO₄*7 H₂O, 1.2 mM Na₂SO₄, 1.3 mM CaCl₂, 0.4 mM KH₂PO₄, 3.5 mM KCl, 120 mM NaCl) containing 0.4% BSA, 10 mM sodium pyruvate, 10 mM glucose and 2 mM glutamine was added to a final volume of 180 µl. Once the probe calibration was completed, the probe plate was replaced by the XF microplate. Three baseline measurements of OCR were measured before sequential application of 6 µM oligomycin, 4 µM FCCP and 2 µM antimycin A in combination with 2 µM rotenone (Sigma-Aldrich, 557368). OCRs were measured by Seahorse XFe96 Flux Analyzer using a mix (30 s), wait (2 min) and measure (3 min) cycle. Each sample was measured in technical replicates. All experiments were conducted independently at least three times. Basal respiration was calculated as the differences between the last OCR measurement before oligomycin injection and the minimum OCR measurement after addition of R/A. Maximal respiration was calculated as the difference between maximum OCR measurement after FCCP injection and the minimum OCR measurement after the addition of R/A. ATP-linked respiration was determined as the difference by the last OCR measurement before oligomycin injection and the minimum OCR measurement after oligomycin injection. Proton leak was determined as the difference between minimum OCR measurement after oligomycin injection and the minimum OCR measurement after the addition of R/A.

Substrate oxidation stress test in synaptosomes

To dissect endogenous substrate consumption, 20 µg of synaptosomal proteins were added to each well in a volume of 80 µl of a

Seahorse XFe96/XF Pro Cell Culture Microplate (Agilent Technologies, 103792-100) coated with polyethylenimine (Sigma-Aldrich, P3143). The mitochondria-loaded XF microplate was centrifuged at 1,900g for 20 min at 4 °C for adherence of the synaptosomes. Pre-warmed assay media (2 mM MgSO₄*7 H₂O, 1.2 mM Na₂SO₄, 1.3 mM CaCl₂, 0.4 mM KH₂PO₄, 3.5 mM KCl, 120 mM NaCl) containing 0.4% BSA, 10 mM sodium pyruvate, 10 mM glucose and 2 mM glutamine was added to a final volume of 180 µl. Etomoxir (Sigma-Aldrich, E1905) was dissolved in dimethylsulfoxide (DMSO) to a 40 mM stock concentration. UK5099 (Sigma-Aldrich, PZO160) was dissolved in DMSO to a 20 mM stock solution. For both inhibitors, 12 µl of stock solution was further dissolved in 3 ml of assay media (2 mM MgSO₄*7 H₂O, 1.2 mM Na₂SO₄, 1.3 mM CaCl₂, 0.4 mM KH₂PO₄, 3.5 mM KCl, 120 mM NaCl) to achieve working solution concentrations of 80 µM UK5099 and 160 µM Etomoxir, that were loaded into the injection ports (resulting in final drug concentrations of 8 µM UK5099 and 16 µM etomoxir in the assay medium). For the control buffer condition, 12 µl DMSO was added to the assay media. Once the probe calibration was completed, the probe plate was replaced by the XF microplate. Three baseline measurements of OCR were measured before application of 8 µM UK5099, 16 µM etomoxir or assay media as control. Thereafter, sequential application of 6 µM oligomycin, 4 µM FCCP and 2 µM antimycin A in combination with 2 µM rotenone followed. OCRs were measured by Seahorse XFe96 Flux Analyzer using a mix (30 s), wait (2 min) and measure (3 min) cycle. OCRs for each genotype were measured independently three times. Each sample was measured in at least ten technical replicates. Within each genotype group, OCR was normalized to the first measurement in the assay and maximal respiration reported as a comparison to the control. Maximal respiration was calculated as the difference between maximum OCR measurement after FCCP injection and the minimum OCR measurement after the addition of R/A.

For measurement of exogenous fatty acid oxidation, 20 µg of synaptosomal proteins were added to each well of a Seahorse XFe96/XF Pro Cell Culture Microplate coated with polyethylenimine. The samples were transferred in substrate-limited assay media (2 mM MgSO₄*7 H₂O, 1.2 mM Na₂SO₄, 1.3 mM CaCl₂, 0.4 mM KH₂PO₄, 3.5 mM KCl, 120 mM NaCl) containing 0.4% BSA, 1 mM sodium pyruvate, 2 mM glucose, 1 mM glutamine and 1 mM carnitine (Sigma-Aldrich, C0283). The mitochondria-loaded XF microplate was centrifuged at 1,900g for 20 min at 4 °C for adherence of the synaptosomes, followed by starvation for 30 min at 37 °C. For assessment of LCFA consumption, palmitate–BSA substrate (Cayman Chemical, 29558) or BSA (Cayman Chemical, 29556) was added to a final concentration of 300 µM palmitate. For assessment of MCFA consumption, heptanoic acid (Sigma-Aldrich, 75190) or octanoic acid (Sigma-Aldrich, C2875) was added at a final concentration of 200 µM. For assessment of SCFA consumption, acetic acid (Sigma-Aldrich, 338826) or butyric acid (Sigma-Aldrich, B103500) was added to the final concentration of 100 µM. Assay medium alone was used as a control for all experiments. For glucose deprivation conditions, neither glucose, pyruvate nor glutamine was added. Instead, palmitate–BSA substrate was added to a final concentration of 300 µM palmitate 2 h before glucose withdrawal. Once the probe calibration was completed, the probe plate was replaced by the XF microplate. Three baseline measurements of OCR were measured before sequential injection of 6 µM oligomycin, 4 µM FCCP and 2 µM antimycin A in combination with 2 µM rotenone. OCR was measured by Seahorse XFe96 Flux Analyzer using a mix (30 s), wait (2 min) and measure (3 min) cycle. All experiments were conducted independently at least three times with each sample measured in at least eight replicates. The maximal respiration was reported as a comparison to the BSA or assay media treatment within each genotype group. Maximal respiration was calculated as the differences between maximum OCR measurement after FCCP injection and the minimum OCR measurement after addition of R/A.

Metabolic analysis of synaptosomes

To dissect TCA metabolites, 1,000 µg of synaptosomal proteins were incubated with 300 µM $^{13}\text{C}_{16}$ palmitate (Cambridge Isotope Laboratories, CLM-3943) or assay media (control) in substrate-limited media (2 mM $\text{MgSO}_4 \cdot 7\text{H}_2\text{O}$, 1.2 mM Na_2SO_4 , 1.3 mM CaCl_2 , 0.4 mM KH_2PO_4 , 3.5 mM KCl, 120 mM NaCl) containing 0.4% BSA, 1 mM sodium pyruvate, 2 mM glucose, 1 mM glutamine and 1 mM carnitine (Sigma-Aldrich, C0283) for 2 h and quenched by snap freezing the samples. Metabolite extraction was carried out in five volumes of 80% methanol for 1 h at -20°C followed by centrifugation at 21,000g at 4°C for 10 min. The supernatants were transferred into new vials for drying in a vacuum centrifuge. Dried extracts were resuspended in 0.1% formic acid before analysis. Targeted measurements on the resuspended metabolite samples were performed on a UPLC-HR-TOF-MS system with an ACQUITY I-Class UPLC (Waters Cooperation) equipped with an ACQUITY UPLC HSS T3 C18 column (2.1 mm \times 100 mm, 1.8 µm, Waters) and coupled to a Bruker maXis Impact QTOF mass spectrometer (Bruker Daltonics). The mobile phase consisted of 0.1% formic acid in water (A) and 0.1% formic acid in methanol:acetonitrile (1:1 vol/vol) (B). The flow rate was set to 0.4 ml min^{-1} at a column temperature of 50°C with the following 21-min gradient: 0% B (0–2 min), 0–40% B (2–6 min), 40–60% B (6–6.5 min), 60–88% B (6.5–11 min), 88–100% (11–11.5 min), 100% B (11.5–18 min), 100–0% B (18–19.5 min) and 0% B (19.5–21 min). The samples were kept at a temperature of 6°C . The QTOF-MS instrument operated in electrospray ionization negative mode, using a capillary voltage of 2.5 kV. The nebulizer gas pressure was 1.2 bar, and the drying gas flow and temperature were 8.0 l min^{-1} and 220°C . The injection volume was 10 µl, and a mass range of 50–1,000 m/z and a sampling rate of 4 Hz were used. Calibration was performed at the end of each run using sodium formate. A mixture of TCA metabolites was included to verify the retention. Bruker Compass Target Analysis (3.1) was used for processing data for extracted ion chromatograms and peak area. Bruker Compass Data Analysis (4.1) was used for inspection of the data.

Substrate oxidation stress test in iPS cell-derived human neurons

On day 7 of differentiation, cortical iNs were dissociated into a cell suspension using Accutase and plated at a density 1×10^5 cells per well in Matrigel-coated Seahorse XFe96/XF Pro 96-well microplates using 100 µl per well of Seahorse XF DMEM medium supplemented with 10 mM glucose, 10 mM sodium pyruvate, 2 mM glutamine and 10 µM Rock inhibitor. Once the probe calibration was completed, the probe plate was replaced by the XF microplate. Three baseline measurements of OCR were carried out before injection of 8 µM UK5099 or 16 µM etomoxir. Seahorse XF DMEM assay medium was used as control. Thereafter, 6 µM oligomycin, 4 µM FCCP and 2 µM antimycin A in combination with 2 µM rotenone were injected sequentially. OCRs were measured by Seahorse XFe96 Flux Analyzer using a mix (30 s), wait (2 min) and measure (3 min) cycle. OCRs for each genotype were measured independently at least three times with each sample being measured in at least eight technical replicates. The total cell numbers in the XF microplate wells were determined by fluorescence imaging with Hoechst on a designated area of the well using BioTek Instrument Cytation 5. Within each genotype group, respiration was normalized to the first measurement, and the maximal respiration was reported as a comparison to the control condition. Maximal respiration was calculated as the difference between maximum OCR measurement after FCCP injection and the minimum OCR measurement after the addition of R/A.

To test the impact of the PPAR α agonist bezafibrate (Sigma-Aldrich, B7273) on neuronal respiration, the drug was dissolved in DMSO to a 10 mM stock solution that was stored at -20°C . On day 5 of neuronal differentiation, half of the cell medium was replaced with medium containing bezafibrate to achieve a final concentration of 10 µM, 50 µM or 100 µM. After 48 h of incubation, iNs were dissociated with accutase

and plated in Matrigel-coated Seahorse XFe96/XF Pro (Agilent) 96-well microplates at a density of 1.5×10^5 iNs per well, and subjected to a substrate oxidation stress test using 16 µM etomoxir as described above.

Statistical analysis of bioenergetic assay data

Seahorse XFe96 Flux Analyzer data were processed in Wave 2.6.1 software (Agilent Technologies) following the manufacturer's guidelines. Raw data were exported from the Wave Software to Prism 10 (GraphPad) for statistical analysis. The number of samples per group is referring to independent analyses (individual animals or neuronal cell cultures) indicated in the corresponding figure legends. The unpaired, two-tailed Student's *t*-test was used to determine statistical significance between the mean values of two groups. Two-way ANOVA with Tukey's post hoc test was used to compare the mean values of all four genotypes.

Electron microscopy

Neurons and isolated synaptosomes were fixed at room temperature for 2 h with 4% (wt/vol) formaldehyde, 2.5% (vol/vol) glutaraldehyde (Sigma-Aldrich G5882) in 0.1 M HEPES pH 7.4, followed by 2 days of fixation at 4°C . Thereafter, the samples were washed with Milli-Q water and pellets, obtained by centrifugation for 5 min at 300g, were embedded in 3% (wt/vol) aqueous agarose (Sigma-Aldrich A4018). Agarose-stabilized samples were cut into 0.5–1-mm³ cubes and prepared for electron microscopy.

Neuronal samples were processed using a modified version of the rOTO protocol as described (<https://www.protocols.io/view/preparation-of-biological-tissues-for-serial-block-36wgq7je5vk5/v2/>). In brief, the samples were postfixed on ice for 1 h with osmium tetroxide reduced with potassium ferrocyanide in 0.1 M sodium cacodylate buffer pH 7. The final concentration was 1% (vol/vol) osmium tetroxide and 1.5% (wt/vol) potassium ferrocyanide in 0.1 M sodium cacodylate buffer. The reduced osmium solution was washed with Milli-Q water and the samples were incubated in 0.1% (wt/vol) aqueous thiocarbohydrazide. After rinsing with water, the samples were incubated for 30 min at room temperature in 1% (vol/vol) osmium tetroxide. Final contrast was achieved by incubating in 2% (wt/vol) uranyl acetate for 30 min at room temperature. After dehydration through a graded series of acetone, embedding was done in Durcupan ACM resin (Sigma-Aldrich). The blocks were polymerized for 48 h at 60°C . Synaptosome samples were postfixed for 2 h at room temperature using 1% (vol/vol) aqueous osmium tetroxide. Then, the samples were rinsed with Milli-Q water and incubated for 2 h at 4°C in 2% (wt/vol) uranyl acetate. Dehydration using a graded ethanol series followed by propylene oxide incubation and resin infiltration with Polybed812 epoxy resin (Polysciences). Blocks were polymerized for 48 h at 60°C .

Ultrathin 80-nm resin sections were sectioned using a Reichert Ultracut S ultramicrotome and picked up on Formvar-coated transmission electron microscopy grids. Reynolds Lead Citrate 3% (Delta Microscopies) was used for post-staining of the sections. Synaptosomes were imaged using a Zeiss EM910 80-kV Transmission Electron Microscope equipped with a 11 M Quemesa CCD camera (EMSIS). Neurons were imaged using the Helios 5 Hydra CX Dual Beam system (Thermo Scientific) operating at 2 kV and 0.4-nA beam current. Micrographs were recorded using the CBS detector for back-scattered electrons and acquisition was done with the MAPS software package, version 3.27 (Thermo Scientific).

Generation of human iPS cell-derived astrocytes (iAs)

Human astrocytes were generated from iPS cells as described²⁷. Briefly, iPS cells were dissociated with Accutase and replated at a density of 5×10^5 cells per well in Matrigel-coated six-well plates using E8 Flex media supplemented with 10 µM Rock inhibitor (Y27632, Cayman Chemical). One day later (day -1), lentivirus vectors were added in fresh E8 Flex medium containing 8 µg ml^{-1} Polybrene (Millipore). The next day (day 0), the medium was replaced with E8 Flex medium containing

doxycycline ($2.5 \mu\text{g ml}^{-1}$; Cayman Chemical), which was kept in the medium until the end of the experiment. On days 1 and 2, cells were cultured in expansion medium (DMEM/F12, 1% N2, 1% Glutamax and 10% FBS), containing $1.25 \mu\text{g ml}^{-1}$ puromycin and $200 \mu\text{g ml}^{-1}$ hygromycin to select for cells containing lentivirus vectors expressing *Sox9* and *Nfib* (provided by the MDC Technology Platform Pluripotent Stem Cells). On days 3–5, the expansion medium was gradually exchanged to FGF medium (Neurobasal medium containing 2% B27, 1% NEAA, 1% Glutamax, 1% FBS and 8 ng ml^{-1} human FGF (PeproTech), 5 ng ml^{-1} human CNTF (PeproTech) and 10 ng ml^{-1} human BMP4 (PeproTech)). On day 6, the cell medium was replaced with fresh FGF medium before the cells were dissociated with Accutase and replated in 2×10^5 cells per well on Matrigel-coated six-well plates on day 7 using FGF medium (supplemented with $10 \mu\text{M}$ Rock inhibitor until day 8). From days 10 to 17, half of the medium was exchanged every second day with maturation medium (1:1 DMEM/F12 and Neurobasal medium containing, 1% N2, 1% Glutamax, 1% sodium pyruvate, $5 \mu\text{g ml}^{-1}$ *N*-acetyl cysteine, $500 \mu\text{g ml}^{-1}$ dbcAMP, 5 ng ml^{-1} EGF-like growth factor, 10 ng ml^{-1} CNTF and 10 ng ml^{-1} BMP4 (PeproTech)). On days 18 and 19, the medium was switched to NB-B27 (Neurobasal medium containing 2% B27 and 1% Glutamax). Astrocytes were kept in culture for up to 30 days, by replacing half of the medium every 2 days.

Conditioned medium to supplement iPS cell-derived human neurons was generated from astrocytes between days 21 and 28 of culture by collecting half of cell medium from each well every second day. Media samples from multiple wells collected the same day were pooled and centrifuged at 300g for 5 min to remove cell debris. Before adding to neurons, the conditioned medium was diluted at a 1:1 ratio with fresh NB-B27 medium and supplemented with 10 ng ml^{-1} human BDNF, 10 ng ml^{-1} human NT3 and 4 mM cytosine β -D-arabinofuranoside. If not used immediately, conditioned media were stored at 4°C for a maximum time of 3 days before addition to iNs.

Generation of human iPS cell-derived neurons

iNs were generated from iPS cells as described previously²⁸. Briefly, iPS cells were dissociated with Accutase and replated at a density of 5.5×10^4 cells per cm^2 in Matrigel-coated 24-well or 12-well plates or 4.3×10^4 cells per cm^2 in Matrigel-coated six-well plates and 100-mm dishes using E8 Flex media supplemented with $10 \mu\text{M}$ Rock inhibitor (Y27632, Cayman Chemical). The next day (day -1), iPS cells were transduced with lentivirus vectors in fresh E8 Flex medium containing $7 \mu\text{g ml}^{-1}$ Polybrene (Millipore). One day after infection (day 0), the medium was replaced with F12-N2 (DMEM/F12, 1% N2, 1% NEAA (Gibco)), containing $2 \mu\text{g ml}^{-1}$ doxycycline, 10 ng ml^{-1} human BDNF (R&D Systems), 10 ng ml^{-1} human NT3 and $0.2 \mu\text{g ml}^{-1}$ mouse laminin (Thermo Fisher). Doxycycline was retained in the medium through the experiment. On day 1, the medium was replaced with fresh F12-N2 medium containing $1 \mu\text{g ml}^{-1}$ puromycin to select vector expressing *Ngn2* (kindly provided by T. Sudhof, Stanford Medicine). At day 2, astrocyte-conditioned medium (iAsCM), prepared as described above, was added and half of the medium exchanged with fresh iAsCM every second day. Alternatively, on day 2, primary glia dissociated in NB-B27 medium (supplemented with $2 \mu\text{g ml}^{-1}$ doxycycline, 10 ng ml^{-1} human BDNF, 10 ng ml^{-1} human NT3 and 4 mM cytosine β -D-arabinofuranoside) were added and half of the medium replaced every 2–3 days. iNs were kept for up to 12 days in culture.

Lipid analyses of cultured human neurons

For fatty acid profiling, 30 mg of cell lysates were hydrolysed with $100 \mu\text{l}$ 10 mol l^{-1} NaOH within 60 min at 80°C in the presence of butylated hydroxytoluene. The samples were neutralized with $100 \mu\text{l}$ acetic acid (58%). A $50 \mu\text{l}$ aliquot was diluted at a 1:10 ratio with methanol containing deuterated internal standards (C12:0-d23, C18:0-d35, C18:2-d4, C20:4-d11, C20:5-d5, C22:0-d43, C22:6-d5, C24:0-d4; 10 ng each; Cayman Chemical). HPLC measurements were performed using

an Agilent 1290 HPLC system with binary pump, autosampler and column thermostat equipped with a Phenomenex Kinetex-C18 column ($2.6 \mu\text{m}$, $2.1 \times 150 \text{ mm}$; Phenomenex) using a solvent system of acetic acid (0.05%) and acetonitrile. The solvent gradient started at 5% acetonitrile and was increased to 98% within 23 min and kept until 26 min with a flow rate of 0.4 ml min^{-1} and $1 \mu\text{l}$ injection volume. The HPLC was coupled with an Agilent 6470 triple-quadrupole mass spectrometer with electrospray ionization source and operated in negative multiple reaction monitoring mode. At least two mass transitions were detected for each fatty acid.

For eCB profiling, 10 mg cell lysates were homogenized in $300 \mu\text{l}$ distilled water. Then, $25 \mu\text{l}$ citric acid (0.4 mol l^{-1}), $10 \mu\text{l}$ of internal standards ($10 \mu\text{g ml}^{-1}$ docosahexaenoic acid-ethanolamid-D4, anandamid-D4, EPA-ethanolamid-D4; Cayman Chemical) and 1 ml ethyl acetate were added. The samples were shaken for 10 min, centrifuged for 3 min at 3,500 rpm and the upper phase recovered. Next, 1 ml ethyl acetate were added to the lower (sample) phase, followed by shaking for further 10 min and centrifugation for 3 min at 3,500 rpm. Again, the upper phase was recovered and both supernatants combined. The solvent was removed to dryness at 40°C under a stream of N_2 , before the residue was resuspended in $100 \mu\text{l}$ acetonitrile and eCB measured. HPLC measurement was performed using an Agilent 1290 HPLC system with binary pump, autosampler and column thermostat equipped with an Agilent Poroshell EC120-C18 column ($2.7 \mu\text{m}$, $2.1 \times 100 \text{ mm}$ column; Agilent) using a solvent system of ammonium format (5 mM) and formic acid (0.05%) in water and methanol. The solvent gradient started at 5% methanol and was increased to 95% within 11 min under gradient conditions and kept until 15 min with a flow rate of 0.4 ml min^{-1} and a $5 \mu\text{l}$ injection volume. The HPLC was coupled with an Agilent 6495 triple-quadrupole mass spectrometer with electrospray ionization source and operated in positive multiple reaction monitoring mode. Two mass transitions per compound were detected. All concentrations were calculated using Agilent Mass Hunter software with individual calibration curves for each compound. All standards were purchased from Cayman Chemical.

Analysis of electrical activity of iNs using MEAs

For MEAs, iPS cells were plated at a density of 4.3×10^4 cells per cm^2 on Matrigel-coated 10-cm dishes and differentiated to iNs as described above. On day 2, cells were dissociated using Accutase and replated at 5×10^5 or 2.5×10^5 cells per well on Multi Channel Systems 24-well plates (24W300/30G-288) in NB-B27 medium supplemented with $10 \mu\text{M}$ Rock inhibitor (Y27632, Cayman Chemical). On day 3, half of the medium was replaced with primary mouse astrocytes at a density $0.5\text{--}0.625 \times 10^5$ cells per well. Astrocyte-enriched cultures were prepared essentially as described⁸⁶. Afterwards, half of the medium was replaced every 2–3 days. Neuronal electrical activity was assessed using the MEA system (MCS) starting from day 14, with recordings taken every 2 days. When network bursts were detectable in most of the wells (~day 38), half of the medium was replaced with NB-B27 medium containing 25 mM glucose, 0.23 mM sodium pyruvate and 2 mM glutamine in the absence or presence of $100 \mu\text{M}$ palmitate. After 6 h of incubation, electrical activity was recorded (pretreatment condition). Following this, the entire medium was replaced by NB-B27 medium lacking glucose, sodium pyruvate and glutamine (Neurobasal-A medium containing 2% B27, $2 \mu\text{g ml}^{-1}$ doxycycline, 10 ng ml^{-1} human BDNF, 10 ng ml^{-1} human NT3 and 4 mM cytosine β -D-arabinofuranoside), in the absence or presence of $100 \mu\text{M}$ palmitic acid. MEA recordings were performed after every 24 h for 3 days.

Spontaneous electrical activity of neurons cultured on MEA plates was recorded at 37°C using Multiwell-Screen software (Multi Channels Systems v.2.0.11.0) for 5 min. Before recording, cells were allowed to stabilize for 5 min. Signals were sampled at 20 kHz, with a 3,500-Hz low-pass and 100-Hz high-pass filter. A spike was detected when the signal went above or below 5% of the baseline noise's standard deviation

during quiet periods. Neuronal burst activity was characterized by the following criteria⁸⁷: a minimum duration of 50 ms with more than four spikes counts; the maximum interval to start and end burst was 50 ms; the minimum interval between bursts was 100 ms. A network burst was recognized when a burst was recorded in at least three channels simultaneously, with a minimum of six channels participating in the activity. Data analysis was limited to active electrodes that detected at least ten spikes per minute, with a minimum amplitude of 20 μ V. The results were analysed using Multi Channel Analyzer (Multi Channel Systems, v.2.0.6.0), where signals from all active electrodes in each well were averaged for plotting. The number of wells for each condition is indicated by an n value.

Protein expression analysis

Mouse synaptosomes or iPSC cell-derived cell types were lysed in RIPA buffer (50 mM Tris-HCl pH 7.4, 150 mM NaCl, 0.5% sodium deoxycholate, 0.1% SDS 1% NP-40) containing complete protease inhibitor cocktail (1 \times ; Roche). Protein concentrations were determined by BCA Protein Assay Kit (Pierce) and equal amounts of proteins or equal volumes of iAsCM were subjected to standard SDS-PAGE, followed by transfer to PVDF membranes. Where applicable, No-Stain Protein Labelling Reagent (Invitrogen) was used to confirm equal transfer between samples. Membranes were blocked for 45 min with 5% milk powder in TBS containing 0.5% Tween-20 and incubated primary antibodies (Supplementary Table 1) overnight at 4 $^{\circ}$ C, followed by incubation with horseradish peroxidase-conjugated secondary antibody (diluted at 1:5,000) for 90 min at room temperature. Immunoreactive bands in cell extracts were visualized using ECL Western Blotting Detection Reagent (Amersham) on iBright CL1500 Imaging System (Invitrogen). For mouse synaptosomal extracts, immunoreactive signals were visualized using SuperSignal West Femto Maximum Sensitivity Substrate (Thermo Scientific). Densitometric analyses were performed using Fiji software.

Immunocytochemistry

For immunocytochemical analysis, cells were plated on Matrigel-coated 13-mm-diameter glass slides in 24-well plates. For analysis, the cells were washed with PBS and fixed in 4% paraformaldehyde in PBS for 20 min, followed by treatment in PBS-based blocking/permeabilization solution containing 0.1% Triton X-100 and 5% donkey serum for 1 h at room temperature. Primary antibody dilutions (Supplementary Table 1) were applied overnight at 4 $^{\circ}$ C in PBS. Thereafter, the cells were washed twice in PBS and once in PBST, followed by incubation with Alexa Fluor-conjugated secondary antibodies for 2 h at room temperature (Supplementary Table 1). For nuclear staining, DAPI (Thermo Fisher) diluted in PBS was used. All images were acquired on a Zeiss LSM 780 or LSM 800 confocal microscope and analysed using Fiji software.

Analysis of gene transcription levels

Total RNA was extracted from tissue or cells using RNeasy Mini/Micro Kit (Qiagen), treated with RNase-Free DNase Set (Qiagen), and reverse transcribed using the High Capacity RNA-to-cDNA Kit (Applied Biosystems) according to the manufacturers' protocols. qPCR were carried out using the TaqMan Fast Advanced Master Mix (Applied Biosystems) and TaqMan assays using QuantStudio 7 Flex Real-Time PCR System (Applied Biosystems) or QuantStudio 6 Pro Real-Time PCR System (Applied Biosystems). TaqMan assay details are listed in Supplementary Table 2. The fold change in transcript levels was calculated using the cycle threshold (CT) comparative method ($2^{-\Delta\Delta CT}$) normalizing to CT values of the internal control gene *GAPDH/Gapdh*. Samples were run in triplicates and non-template reaction served as negative controls.

To assess the pluripotency of iPSC cell lines, the TaqMan hPS cell Scorecard Assay (Applied Biosystems) was used according to the manufacturer's instructions. RNA extraction and cDNA reverse transcription of 1 μ g of total RNA was performed as described above. The scorecard

assay was run in a 384-well format on the QuantStudio 7 Flex Real-Time PCR System using the Standard Curve Method. Gene expression data were analysed using the web-based hPS cell Scorecard Analysis Software (Thermo Fisher Scientific).

The expression of 84 PPAR target genes was assessed using the Human PPAR Targets RT² Profiler PCR Array (Qiagen; 384-well format) according to the manufacturer's instructions. RNA was extracted using the RNeasy Mini/Micro Kit (Qiagen), treated with RNase-Free DNase Set (Qiagen) and reverse transcribed with RT² First Strand Kit (Qiagen). qPCR was performed using RT² SYBR Green ROX qPCR Mastermix (Qiagen) on a QuantStudio 7 Flex Real-Time PCR System (Applied Biosystems). The comparison of transcript levels was calculated using the $2^{-\Delta\Delta CT}$ method normalizing to CT values of internal control gene *GAPDH*. Data analysis was conducted with the web-based GeneGlobe Data Analysis Center (<https://geneglobe.qiagen.com/>). Changes in mRNA levels in E3KO and E4KO cells were assessed as compared to the respective isogenic WT controls. Genes with more than a 2-fold difference in expression were considered to be differentially expressed. Two arrays were run for each E3WT-versus-E3KO and E4WT-versus-E4KO comparison, and genes showing the same changes in both arrays were chosen for further validation with TaqMan RT-qPCR assays.

Gene expression analysis in sorted mouse neurons and astrocytes

A detailed description of cell sorting of mouse cortices has been published⁸⁸. Briefly, brain regions were dissected, enzymatically digested with papain and applied to LS columns for myelin removal (Miltenyi Biotec). The resulting cell suspension was labelled with the following antibodies: microglia/macrophages (CD45-BV421; 1:200 dilution, BD Biosciences, 563890), endothelial cells (CD49a-FITC; 1:200 dilution, Miltenyi Biotec, 130-107-636), oligodendrocytes (O4-PE; 1:200 dilution, Miltenyi Biotec, 130-117-357) and astrocytes (ACSA2-APC, 1:100 dilution, Miltenyi Biotec, 130-116-245) before sorting with BD Aria Fusion. The individual cell populations were tested for purity using qPCR probes for astrocytes testing for *Gfap* (Mm01253033_m1) and *Aldh1l1* (Mm03048949_m1) and for neurons using *NeuN/Rbfox3* (Mm01248771_m1) and *Bqf53b/Actl6b* (Mm00504274_m1). Gene expression analyses were performed using the following probes: *Acaadl* (Mm00599660_m1), *CRAT* (Mm00483985_m1), *Cpt1a* (Mm-01231183_m1), *Cpt2* (Mm00487202_m1), *Acadvl* (Mm00444293_m1), *Acadm* (Mm00431611_m1), *Slc16a1* (Mm01306379_m1) and *Slc22a5* (Mm00441468_m1). *Gapdh* (Mm99999915_g1) served as the housekeeping gene.

Analysis of mitochondria structure

For quantification of the amounts of mitochondria in iNs, the cells were cultured on Matrigel-coated 13-mm-diameter glass slides in 24-well plates and incubated with 100 nM MitoTracker Red CMXRos (Invitrogen) for 30 min. After staining, cells were washed with fresh medium and fixed in 4% paraformaldehyde in PBS for 20 min. Images were acquired using a Zeiss LSM 800 confocal microscope. z-stack images (14 slices; interval 0.2 μ m) were analysed using Fiji software. To measure cell body area, GFP signal was used to manually track each cell body shape. Images of mitochondria were binarized and thresholding parameters adjusted based on the MitoTracker signal. The particle analysis function was used to measure mitochondria area obtained by pixels that make up the MitoTracker signal. The fraction of the total GFP-positive cell area occupied by MitoTracker Red⁺ mitochondria was obtained by dividing total mitochondria area by cell area.

Mitochondrial morphology was assessed using electron microscopy images. Quantitative analysis of mitochondrial shape was performed in Fiji by manually outlining individual mitochondria to measure mitochondrial area and circularity. A total of 299–347 mitochondria from 60–62 images per genotype were analysed for synaptosomes, and 39–78 mitochondria from 5–6 images per genotype were used for neurons.

APOE genotyping

Genomic DNA was extracted from stem cells using Wizard Genomic DNA Purification Kit (Promega). APOE genotyping was carried out using the TaqMan SNP Genotyping Assay and TaqMan Genotyping Master Mix (Applied Biosystems) on a QuantStudio 7 Flex Real-Time PCR System (Applied Biosystems). Genotypes were determined based on single nucleotide polymorphism rs429358 that defines the ε3 and ε4 alleles of human APOE (assay ID C_3084793_20; Applied Biosystem). FAM and VIC reporter dyes were used for allele discrimination.

Statistical analysis

Statistical analyses were performed using GraphPad Prism. The applied statistical tests and the number *n* (sample size) are indicated in each figure legend. Data are presented as the mean ± s.d., unless otherwise stated in the respective figure legends. Where applicable, outliers were determined using Grubbs' test or the ROUT method (*Q* = 1).

Reporting summary

Further information on research design is available in the Nature Portfolio Reporting Summary linked to this article.

Data availability

All uncropped images of immunoblots are published alongside the paper. Additional data on dose range findings will be made available by the corresponding author on request. Source data are provided with this paper.

References

- Jansen, P. et al. Roles for the pro-neurotrophin receptor sortilin in neuronal development, aging and brain injury. *Nat. Neurosci.* **10**, 1449–1457 (2007).
- Musunuru, K. et al. From noncoding variant to phenotype via SORT1 at the 1p13 cholesterol locus. *Nature* **466**, 714–719 (2010).
- Kjolby, M. et al. Sort1, encoded by the cardiovascular risk locus 1p13.3, is a regulator of hepatic lipoprotein export. *Cell Metab.* **12**, 213–223 (2010).
- Malik, A. R. & Willnow, T. E. VPS10P domain receptors: sorting out brain health and disease. *Trends Neurosci.* **43**, 870–885 (2020).
- Salasova, A., Monti, G., Andersen, O. M. & Nykjaer, A. Finding memo: versatile interactions of the VPS10p-domain receptors in Alzheimer's disease. *Mol. Neurodegener.* **17**, 74 (2022).
- Carlo, A. S., Nykjaer, A. & Willnow, T. E. Sorting receptor sortilin-a culprit in cardiovascular and neurological diseases. *J. Mol. Med.* **92**, 905–911 (2014).
- Kathiresan, S. et al. Common variants at 30 loci contribute to polygenic dyslipidemia. *Nat. Genet.* **41**, 56–65 (2009).
- Strong, A. et al. Hepatic sortilin regulates both apolipoprotein B secretion and LDL catabolism. *J. Clin. Invest.* **122**, 2807–2816 (2012).
- Linsel-Nitschke, P. et al. Genetic variation at chromosome 1p13.3 affects sortilin mRNA expression, cellular LDL-uptake and serum LDL levels which translates to the risk of coronary artery disease. *Atherosclerosis* **208**, 183–189 (2010).
- Carlo, A. S. et al. The pro-neurotrophin receptor sortilin is a major neuronal apolipoprotein E receptor for catabolism of amyloid-beta peptide in the brain. *J. Neurosci.* **33**, 358–370 (2013).
- Herz, J. Apolipoprotein E receptors in the nervous system. *Curr. Opin. Lipidol.* **20**, 190–196 (2009).
- Holtzman, D. M., Herz, J. & Bu, G. Apolipoprotein e and apolipoprotein e receptors: normal biology and roles in Alzheimer disease. *Cold Spring Harb. Perspect. Med.* **2**, a006312 (2012).
- Bu, G. Apolipoprotein E and its receptors in Alzheimer's disease: pathways, pathogenesis and therapy. *Nat. Rev. Neurosci.* **10**, 333–344 (2009).
- Asaro, A. et al. Apolipoprotein E4 disrupts the neuroprotective action of sortilin in neuronal lipid metabolism and endocannabinoid signaling. *Alzheimers Dement.* **16**, 1248–1258 (2020).
- Asaro, A. et al. ApoE4 disrupts interaction of sortilin with fatty acid-binding protein 7 essential to promote lipid signaling. *J. Cell Sci.* **134**, jcs258894 (2021).
- Corder, E. H. et al. Gene dose of apolipoprotein E type 4 allele and the risk of Alzheimer's disease in late onset families. *Science* **261**, 921–923 (1993).
- Bellenguez, C. et al. New insights into the genetic etiology of Alzheimer's disease and related dementias. *Nat. Genet.* **54**, 412–436 (2022).
- Carrasquillo, M. M. et al. Genome-wide screen identifies rs646776 near sortilin as a regulator of progranulin levels in human plasma. *Am. J. Hum. Genet.* **87**, 890–897 (2010).
- Gervois, P., Torra, I. P., Fruchart, J. C. & Staels, B. Regulation of lipid and lipoprotein metabolism by PPAR activators. *Clin. Chem. Lab. Med.* **38**, 3–11 (2000).
- Knouff, C. et al. Apo E structure determines VLDL clearance and atherosclerosis risk in mice. *J. Clin. Invest.* **103**, 1579–1586 (1999).
- Khattar, N. K. et al. Isolation of functionally active and highly purified neuronal mitochondria from human cortex. *J. Neurosci. Methods* **263**, 1–6 (2016).
- Hildyard, J. C., Ammala, C., Dukes, I. D., Thomson, S. A. & Halestrap, A. P. Identification and characterisation of a new class of highly specific and potent inhibitors of the mitochondrial pyruvate carrier. *Biochim. Biophys. Acta* **1707**, 221–230 (2005).
- Pike, L. S., Smift, A. L., Croteau, N. J., Ferrick, D. A. & Wu, M. Inhibition of fatty acid oxidation by etomoxir impairs NADPH production and increases reactive oxygen species resulting in ATP depletion and cell death in human glioblastoma cells. *Biochim. Biophys. Acta* **1807**, 726–734 (2011).
- Houten, S. M., Violante, S., Ventura, F. V. & Wanders, R. J. The biochemistry and physiology of mitochondrial fatty acid beta-oxidation and its genetic disorders. *Annu. Rev. Physiol.* **78**, 23–44 (2016).
- Lee, H. et al. ApoE4-dependent lysosomal cholesterol accumulation impairs mitochondrial homeostasis and oxidative phosphorylation in human astrocytes. *Cell Rep.* **42**, 113183 (2023).
- Sarret, P. et al. Distribution of NTS3 receptor/sortilin mRNA and protein in the rat central nervous system. *J. Comp. Neurol.* **461**, 483–505 (2003).
- Canals, I. et al. Rapid and efficient induction of functional astrocytes from human pluripotent stem cells. *Nat. Methods* **15**, 693–696 (2018).
- Zhang, Y. et al. Rapid single-step induction of functional neurons from human pluripotent stem cells. *Neuron* **78**, 785–798 (2013).
- Bedse, G., Romano, A., Lavecchia, A. M., Cassano, T. & Gaetani, S. The role of endocannabinoid signaling in the molecular mechanisms of neurodegeneration in Alzheimer's disease. *J. Alzheimers Dis.* **43**, 1115–1136 (2015).
- O'Sullivan, S. E. An update on PPAR activation by cannabinoids. *Br. J. Pharmacol.* **173**, 1899–1910 (2016).
- Iannotti, F. A. & Vitale, R. M. The endocannabinoid system and PPARs: focus on their signalling crosstalk, action and transcriptional regulation. *Cells* **10**, 586 (2021).
- Kanda, T., Odani, S., Tomoi, M., Matsubara, Y. & Ono, T. Primary structure of a 15-kDa protein from rat intestinal epithelium. Sequence similarity to fatty-acid-binding proteins. *Eur. J. Biochem.* **197**, 759–768 (1991).
- Augustyniak, J. et al. Bezafibrate upregulates mitochondrial biogenesis and influence neural differentiation of human-induced pluripotent stem cells. *Mol. Neurobiol.* **56**, 4346–4363 (2019).

34. Ivancevic, V. et al. Regional cerebral glucose metabolism in healthy volunteers determined by fluorodeoxyglucose positron emission tomography: appearance and variance in the transaxial, coronal, and sagittal planes. *Clin. Nucl. Med.* **25**, 596–602 (2000).
35. Pardo, J. V. et al. Where the brain grows old: decline in anterior cingulate and medial prefrontal function with normal aging. *Neuroimage* **35**, 1231–1237 (2007).
36. Ding, F., Yao, J., Rettberg, J. R., Chen, S. & Brinton, R. D. Early decline in glucose transport and metabolism precedes shift to ketogenic system in female aging and Alzheimer's mouse brain: implication for bioenergetic intervention. *PLoS ONE* **8**, e79977 (2013).
37. Wang, Y. et al. Midlife chronological and endocrinological transitions in brain metabolism: system biology basis for increased Alzheimer's risk in female brain. *Sci. Rep.* **10**, 8528 (2020).
38. Yin, F. et al. The perimenopausal aging transition in the female rat brain: decline in bioenergetic systems and synaptic plasticity. *Neurobiol. Aging* **36**, 2282–2295 (2015).
39. Fattoretti, P. et al. Quantitative immunohistochemistry of glucose transport protein (Glut3) expression in the rat hippocampus during aging. *J. Histochem. Cytochem.* **49**, 671–672 (2001).
40. Willette, A. A. et al. Association of insulin resistance with cerebral glucose uptake in late middle-aged adults at risk for Alzheimer disease. *JAMA Neurol.* **72**, 1013–1020 (2015).
41. Weise, C. M. et al. Left lateralized cerebral glucose metabolism declines in amyloid-beta positive persons with mild cognitive impairment. *Neuroimage Clin.* **20**, 286–296 (2018).
42. Croteau, E. et al. A cross-sectional comparison of brain glucose and ketone metabolism in cognitively healthy older adults, mild cognitive impairment and early Alzheimer's disease. *Exp. Gerontol.* **107**, 18–26 (2018).
43. Jeong, Y. et al. Pattern of glucose hypometabolism in frontotemporal dementia with motor neuron disease. *Neurology* **64**, 734–736 (2005).
44. Diehl-Schmid, J. et al. Decline of cerebral glucose metabolism in frontotemporal dementia: a longitudinal 18F-FDG-PET-study. *Neurobiol. Aging* **28**, 42–50 (2007).
45. Zhang, Y. et al. Ketosis proportionately spares glucose utilization in brain. *J. Cereb. Blood Flow. Metab.* **33**, 1307–1311 (2013).
46. Taib, B. et al. Glucose regulates hypothalamic long-chain fatty acid metabolism via AMP-activated kinase (AMPK) in neurons and astrocytes. *J. Biol. Chem.* **288**, 37216–37229 (2013).
47. Kumar, M. et al. Triglycerides are an important fuel reserve for synapse function in the brain. *Nat. Metab.* **7**, 1392–1403 (2025).
48. Saber, S.H. et al. DDHD2 provides a critical flux of saturated fatty acids to support neuronal energy demands. Preprint at *bioRxiv* <https://doi.org/10.1038/s42255-025-01367-x> (2024).
49. Wei, Y. et al. Aerobic glycolysis is the predominant means of glucose metabolism in neuronal somata, which protects against oxidative damage. *Nat. Neurosci.* **26**, 2081–2089 (2023).
50. Feng, L., Hatten, M. E. & Heintz, N. Brain lipid-binding protein (BLBP): a novel signaling system in the developing mammalian CNS. *Neuron* **12**, 895–908 (1994).
51. Kurtz, A. et al. The expression pattern of a novel gene encoding brain-fatty acid binding protein correlates with neuronal and glial cell development. *Development* **120**, 2637–2649 (1994).
52. Kaczocha, M., Glaser, S. T. & Deutsch, D. G. Identification of intracellular carriers for the endocannabinoid anandamide. *Proc. Natl Acad. Sci. USA* **106**, 6375–6380 (2009).
53. Adida, A. & Spener, F. Adipocyte-type fatty acid-binding protein as inter-compartmental shuttle for peroxisome proliferator activated receptor gamma agonists in cultured cell. *Biochim. Biophys. Acta* **1761**, 172–181 (2006).
54. Mita, R., Beaulieu, M. J., Field, C. & Godbout, R. Brain fatty acid-binding protein and omega-3/omega-6 fatty acids: mechanistic insight into malignant glioma cell migration. *J. Biol. Chem.* **285**, 37005–37015 (2010).
55. Tripathi, S. et al. Docosahexaenoic acid up-regulates both PI3K/AKT-dependent FABP7-PPARgamma interaction and MKP3 that enhance GFAP in developing rat brain astrocytes. *J. Neurochem.* **140**, 96–113 (2017).
56. Moulle, V. S., Cansell, C., Luquet, S. & Cruciani-Guglielmacci, C. The multiple roles of fatty acid handling proteins in brain. *Front. Physiol.* **3**, 385 (2012).
57. Artmann, A. et al. Influence of dietary fatty acids on endocannabinoid and N-acylethanolamine levels in rat brain, liver and small intestine. *Biochim. Biophys. Acta* **1781**, 200–212 (2008).
58. Kozak, K. R. et al. 15-Lipoxygenase metabolism of 2-arachidonylglycerol. Generation of a peroxisome proliferator-activated receptor alpha agonist. *J. Biol. Chem.* **277**, 23278–23286 (2002).
59. Mi, Y. et al. Loss of fatty acid degradation by astrocytic mitochondria triggers neuroinflammation and neurodegeneration. *Nat. Metab.* **5**, 445–465 (2023).
60. Jiang, T. & Cadenas, E. Astrocytic metabolic and inflammatory changes as a function of age. *Aging Cell* **13**, 1059–1067 (2014).
61. Williams, H. C. et al. APOE alters glucose flux through central carbon pathways in astrocytes. *Neurobiol. Dis.* **136**, 104742 (2020).
62. Farmer, B. C. et al. APOE4 lowers energy expenditure in females and impairs glucose oxidation by increasing flux through aerobic glycolysis. *Mol. Neurodegener.* **16**, 62 (2021).
63. Qi, G. et al. ApoE4 impairs neuron-astrocyte coupling of fatty acid metabolism. *Cell Rep.* **34**, 108572 (2021).
64. Windham, I. A. et al. APOE traffics to astrocyte lipid droplets and modulates triglyceride saturation and droplet size. *J. Cell Biol.* **223**, e202305003 (2024).
65. Lindner, K. et al. Isoform- and cell-state-specific lipidation of ApoE in astrocytes. *Cell Rep.* **38**, 110435 (2022).
66. Miranda, A. M. et al. Effects of APOE4 allelic dosage on lipidomic signatures in the entorhinal cortex of aged mice. *Transl. Psychiatry* **12**, 129 (2022).
67. Vaegter, C. B. et al. Sortilin associates with Trk receptors to enhance anterograde transport and neurotrophin signaling. *Nat. Neurosci.* **14**, 54–61 (2011).
68. Teng, H. K. et al. ProBDNF induces neuronal apoptosis via activation of a receptor complex of p75NTR and sortilin. *J. Neurosci.* **25**, 5455–5463 (2005).
69. Hu, F. et al. Sortilin-mediated endocytosis determines levels of the frontotemporal dementia protein, progranulin. *Neuron* **68**, 654–667 (2010).
70. Philtjens, S. et al. Rare nonsynonymous variants in SORT1 are associated with increased risk for frontotemporal dementia. *Neurobiol. Aging* **66**, 181.e3–181.e10 (2018).
71. Lee, W. C. et al. Targeted manipulation of the sortilin-progranulin axis rescues progranulin haploinsufficiency. *Hum. Mol. Genet.* **23**, 1467–1478 (2013).
72. Mosconi, L., Andrews, R. D. & Matthews, D. C. Comparing brain amyloid deposition, glucose metabolism, and atrophy in mild cognitive impairment with and without a family history of dementia. *J. Alzheimers Dis.* **35**, 509–524 (2013).
73. Chen, Y., Durakoglugil, M. S., Xian, X. & Herz, J. ApoE4 reduces glutamate receptor function and synaptic plasticity by selectively impairing ApoE receptor recycling. *Proc. Natl Acad. Sci. USA* **107**, 12011–12016 (2010).
74. Zhao, N. et al. Apolipoprotein E4 impairs neuronal insulin signaling by trapping insulin receptor in the endosomes. *Neuron* **96**, 115–129 (2017).

75. Heeren, J., Beisiegel, U. & Grewal, T. Apolipoprotein E recycling: implications for dyslipidemia and atherosclerosis. *Arterioscler Thromb. Vasc. Biol.* **26**, 442–448 (2006).
76. Heeren, J. et al. Impaired recycling of apolipoprotein E4 is associated with intracellular cholesterol accumulation. *J. Biol. Chem.* **279**, 55483–55492 (2004).
77. Heeren, J. et al. Recycling of apoprotein E is associated with cholesterol efflux and high density lipoprotein internalization. *J. Biol. Chem.* **278**, 14370–14378 (2003).
78. Xian, X. et al. Reversal of ApoE4-induced recycling block as a novel prevention approach for Alzheimer's disease. *Elife* **7**, e40048 (2018).
79. Pohlkamp, T. et al. NHE6 depletion corrects ApoE4-mediated synaptic impairments and reduces amyloid plaque load. *Elife* **10**, e72034(2021).
80. Yamazaki, Y., Zhao, N., Caulfield, T. R., Liu, C. C. & Bu, G. Apolipoprotein E and Alzheimer disease: pathobiology and targeting strategies. *Nat. Rev. Neurol.* **15**, 501–518 (2019).
81. Blumenfeld, J., Yip, O., Kim, M. J. & Huang, Y. Cell type-specific roles of APOE4 in Alzheimer disease. *Nat. Rev. Neurosci.* **25**, 91–110 (2024).
82. Zhang, L., Xia, Y. & Gui, Y. Neuronal ApoE4 in Alzheimer's disease and potential therapeutic targets. *Front. Aging Neurosci.* **15**, 1199434 (2023).
83. Nykjaer, A. et al. Sortilin is essential for proNGF-induced neuronal cell death. *Nature* **427**, 843–848 (2004).
84. Ding, Q. et al. A TALEN genome-editing system for generating human stem cell-based disease models. *Cell Stem Cell* **12**, 238–251 (2013).
85. Ludwik, K. A., Telugu, N., Schommer, S., Stachelscheid, H. & Diecke, S. ASSURED-optimized CRISPR protocol for knockout/SNP knockin in hiPSCs. *STAR Protoc.* **4**, 102406 (2023).
86. Schildge, S., Bohrer, C., Beck, K. & Schachtrup, C. Isolation and culture of mouse cortical astrocytes. *J. Vis. Exp.* **71**, 50079 (2013).
87. Chen, M. et al. Rapid generation of regionally specified CNS neurons by sequential patterning and conversion of human induced pluripotent stem cells. *Stem Cell Res.* **48**, 101945 (2020).
88. Schmidt, V et al. A β -induced distress of astrocytes triggers Alzheimer disease pathology through non-canonical δ secretase activity. Preprint at *bioRxiv* <https://doi.org/10.1101/2025.01.30.635618> (2025).

Acknowledgements

We are indebted to T. Pasternack, K. Kampf, H. Zweers, C. Schiel, K.-M. Pedersen, C. B. Nielsen and A. Højland for expert technical assistance. Studies were funded in part by the European Research Council (BeyOND no. 335692), the Alzheimer Forschung Initiative (18003) and the Novo Nordisk Foundation (NNF18OC0033928) to T.E.W.

Author contributions

A.K.G., J.P.G., E.Z.-P., R.F.-G., V.S.-K., I.-M.R. and N.S.T. designed and conducted the experiments and analysed data. C.G. provided essential expert advice. J.K., S.K., M.R., S.D., P.B., M.J. and T.E.W. conceptualized the study and evaluated data. A.K.G., J.P.G., P.B. and T.E.W. wrote the paper.

Competing interests

The authors declare no competing interests.

Additional information

Extended data is available for this paper at <https://doi.org/10.1038/s42255-025-01389-5>.

Supplementary information The online version contains supplementary material available at <https://doi.org/10.1038/s42255-025-01389-5>.

Correspondence and requests for materials should be addressed to Thomas E. Willnow.

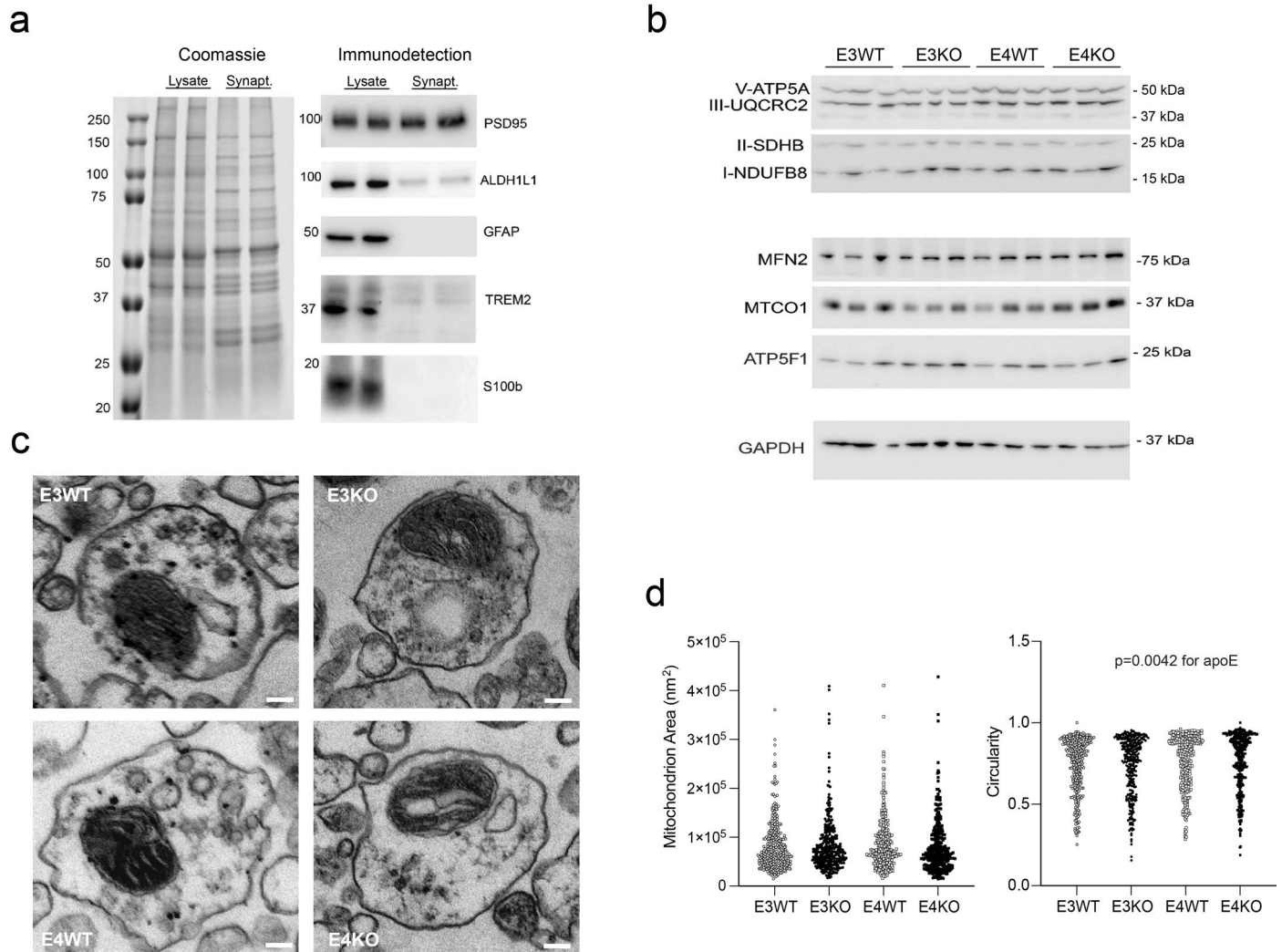
Peer review information *Nature Metabolism* thanks Carlos Manlio Díaz-García and the other, anonymous, reviewer(s) for their contribution to the peer review of this work. Primary Handling Editor: Alfredo Gimenez-Cassina, in collaboration with the *Nature Metabolism* team.

Reprints and permissions information is available at www.nature.com/reprints.

Publisher's note Springer Nature remains neutral with regard to jurisdictional claims in published maps and institutional affiliations.

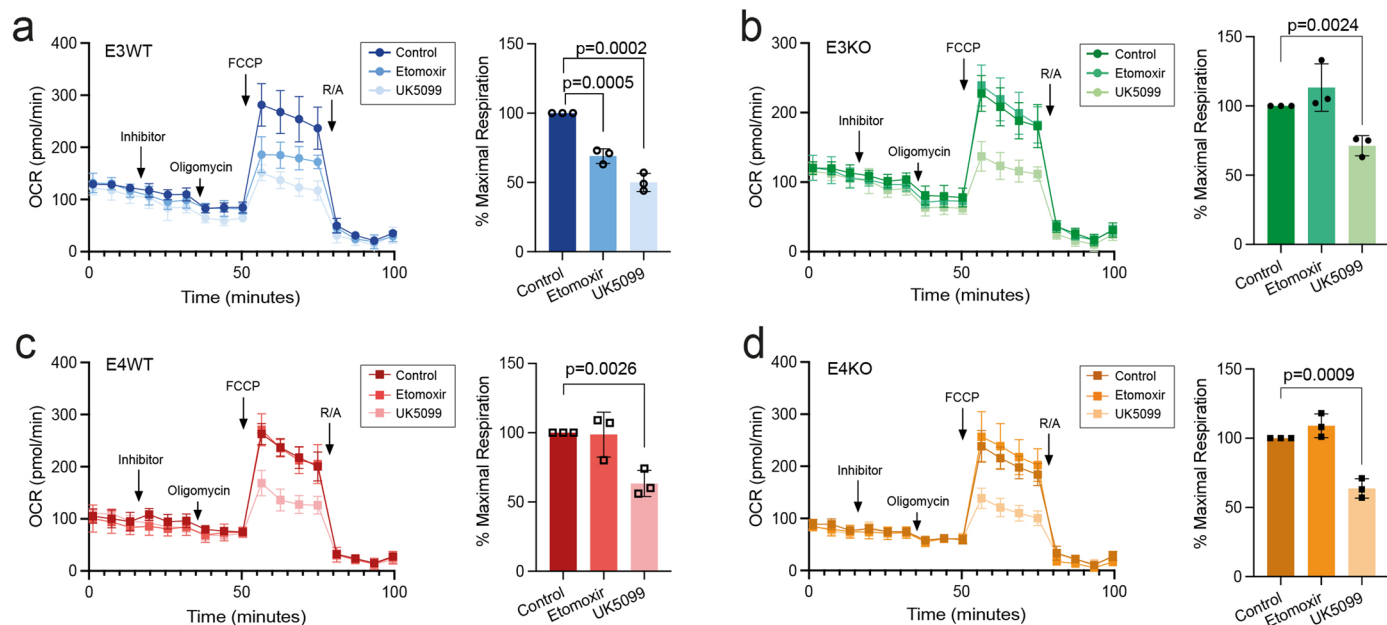
Open Access This article is licensed under a Creative Commons Attribution-NonCommercial-NoDerivatives 4.0 International License, which permits any non-commercial use, sharing, distribution and reproduction in any medium or format, as long as you give appropriate credit to the original author(s) and the source, provide a link to the Creative Commons licence, and indicate if you modified the licensed material. You do not have permission under this licence to share adapted material derived from this article or parts of it. The images or other third party material in this article are included in the article's Creative Commons licence, unless indicated otherwise in a credit line to the material. If material is not included in the article's Creative Commons licence and your intended use is not permitted by statutory regulation or exceeds the permitted use, you will need to obtain permission directly from the copyright holder. To view a copy of this licence, visit <http://creativecommons.org/licenses/by-nc-nd/4.0/>.

© The Author(s) 2025



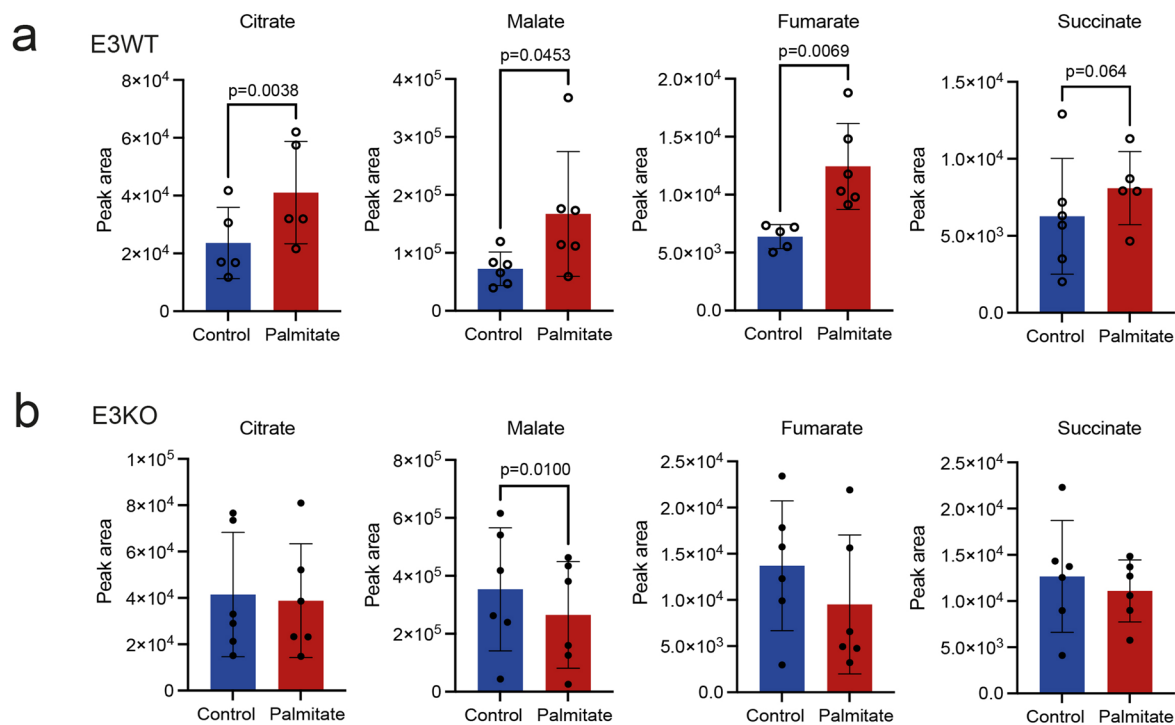
Extended Data Fig. 1 | Structural analysis of mitochondria in synaptosomal preparations of mouse brains. (a) Western blot analysis of neuronal (PSD95) and astrocytic (ALDH1L1, GFAP, TREM2, S100B) marker proteins in total lysate and in synaptosomal preparations of two E3WT mouse brains (right panel) is shown. Coomassie staining was used as a control for equal protein loading (left panel). The migration of molecular weight markers in the gels is indicated (in kDa). Immunosignals for neuronal but not astrocytic markers in synaptosomal preparations confirm absence of glia contamination in these preparations. Data were acquired from two preparations. (b) Western blot analysis of respiratory chain subunits and mitofusin 2 (MFN2) in synaptosomes isolated from mouse brains as in panel a ($n = 3$ animals per group). Five μg synaptosomal lysate were

loaded in each lane. Detection of GAPDH served as loading control. No apparent differences in protein levels are seen comparing genotypes. The experiment was performed in 2-3 independent synaptosomal preparation. (c) Representative electron microscopic images of synaptosomes isolated from E3WT, E3KO, E4WT, or E4KO brain cortices of male mice showing trapped neuronal mitochondria. Scale bars: 100 nm. (d) Morphometric analyses deduced from electron microscopic images exemplified in (c), document comparable values for area of individual mitochondria in the genotype groups, but a subtle effect of *APOE*, but not *Sort1* genotype circularity. A total of 299-347 mitochondria on 60-62 images were analyzed (one EM preparation per genotype). Statistical significance of data was tested using two-way ANOVA with Tukey's multiple comparison test.



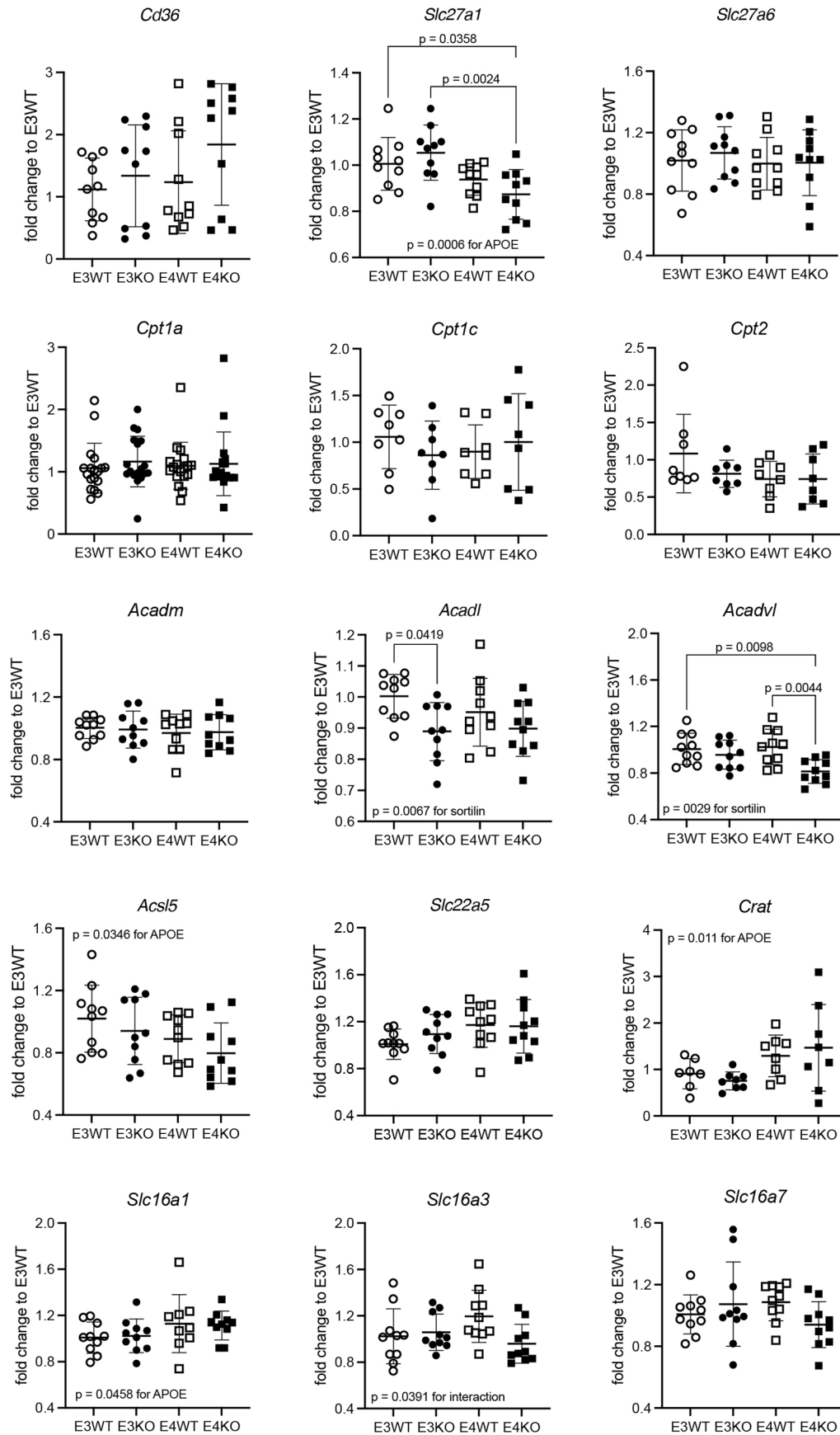
Extended Data Fig. 2 | Loss of sortilin or the presence of apoE4 renders neuronal mitochondria from female mice insensitive to inhibition of long-chain fatty acid import. The dependency of mitochondrial respiration on availability of glucose or long-chain fatty acids was assessed in synaptosomes isolated from the brains of female mice either E3WT (a), E3KO (b), E4WT (c) or E4KO (d) (12 weeks of age) by determination of real-time oxygen consumption rates. The experimental setup replicates the one described in Fig. 1g-j for male mice and includes measurements in the presence of solvent control buffer

(control) or solutions containing 8 μ M UK5099 or 16 μ M etomoxir (inhibitor). For each genotype, one exemplary experiment is shown (to the left) as well as the quantification of % maximal OCR compared to the control condition (set to 100%; to the right). Data are given as mean \pm s.d. from $n = 3$ biological replicates. Each biological replicate data point is the mean of $n = 10-18$ technical replicates. Statistical significance of data was tested using unpaired Student's t test (two-tailed). Individual respiration profiles of three independent experiments are given in Supplementary figure S3.



Extended Data Fig. 3 | Sortilin deficiency blocks consumption of long-chain fatty acids in the TCA cycle. Levels of the indicated tricarboxylic acid cycle metabolites in E3WT (a) and E3KO (b) synaptosomes were assessed by LC-MS in the presence of buffer (control) or after treatment for 2 hours with 300 μ M potassium palmitate. All experiments were performed under low glucose

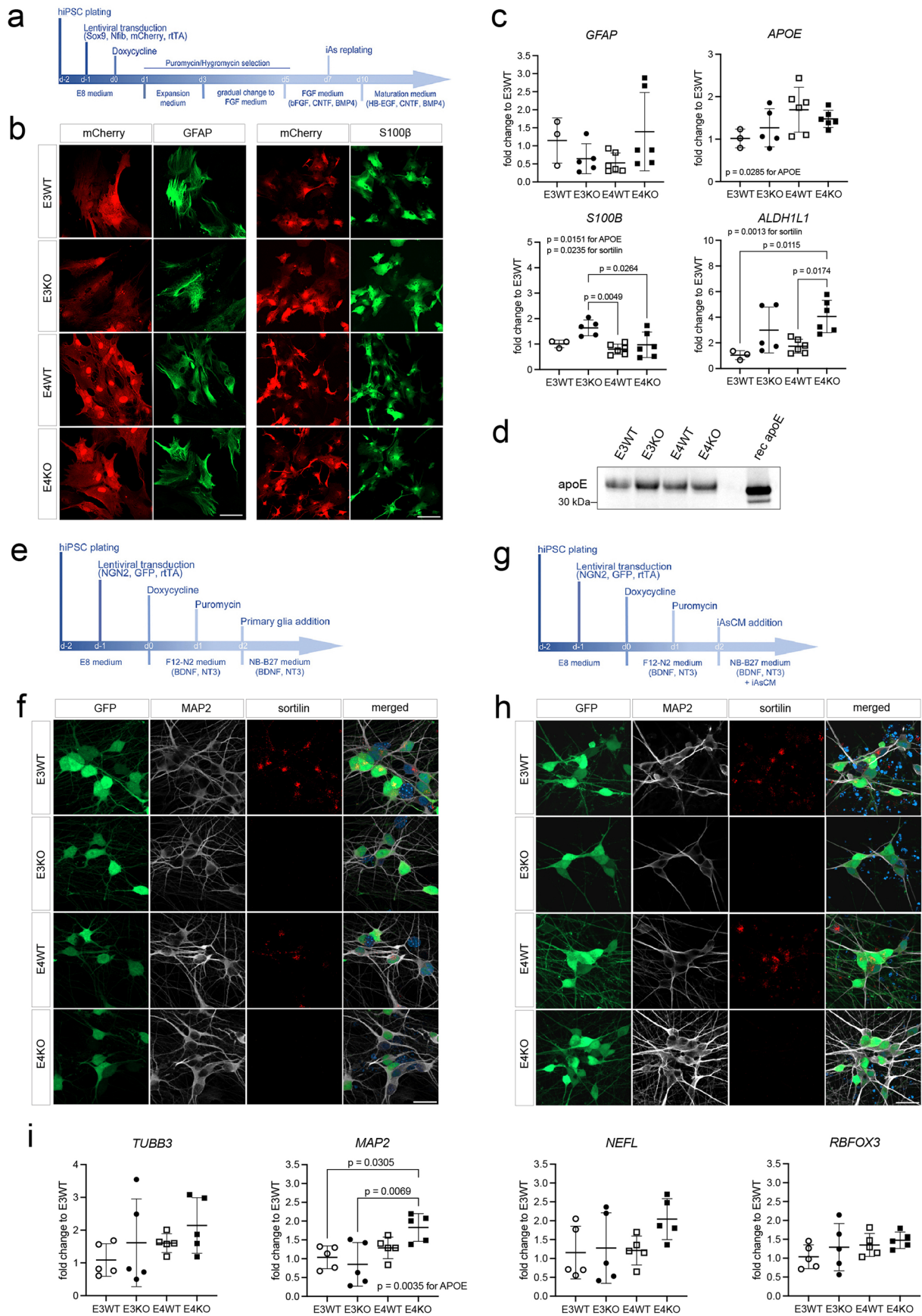
conditions (1 mM sodium pyruvate, 2 mM glucose, 1 mM glutamine). Peak area for each metabolite is reported as mean \pm s.d. of $n = 5$ biological replicates (mice) for E3WT and $n = 6$ for E3KO. Statistical significance of data was tested using paired Student's t test (two-tailed). This experiment was repeated six times.



Extended Data Fig. 4 | See next page for caption.

Extended Data Fig. 4 | Gene expression patterns in mouse cortices related to mitochondrial consumption of long-chain fatty acids. Cortical gene expression patterns were studied in male mice (12 weeks of age) of the indicated *Sort1* and human *APOE* genotypes using quantitative RT-PCR (n = 8-18 animals per group, depending on the gene analyzed). Individual data points as well as the mean \pm s.d. of the entire genotype group are given. Statistical significance of data was tested using two-way ANOVA with Tukey's multiple comparison test. *Acadl*, acyl-CoA dehydrogenase long chain; *Acadm*, acyl-CoA dehydrogenase medium chain; *Acadvl*, acyl-CoA dehydrogenase very long chain; *Acs5*, acyl-CoA

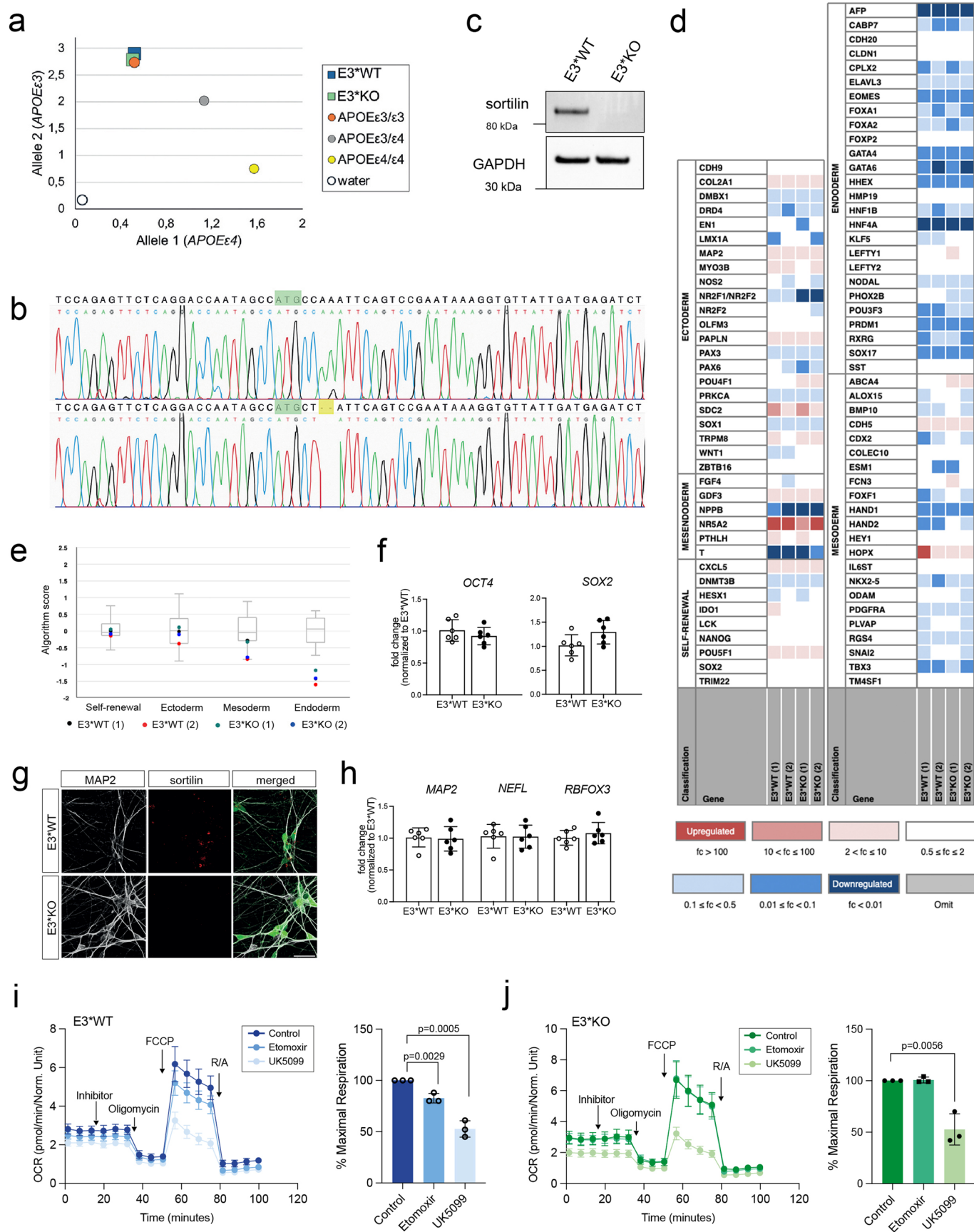
synthetase long chain family member 5; *Cd36*, fatty acid translocase; *Cpt1a*, carnitine *O*-palmitoyltransferase 1 A; *Cpt1c*, carnitine *O*-palmitoyltransferase 1 C; *Cpt2*, carnitine *O*-palmitoyltransferase 2; *Crat*, carnitine *O*-acyltransferase; *Slc16a1*, solute carrier family 16 member 1 encoding monocarboxylate transporter (MCT) 1; *Slc16a3*, solute carrier family 16 member 3 encoding MCT4; *Slc16a7*, solute carrier family 16 member 7 encoding MCT2; *Slc22a5*, solute carrier family 22 member 5; *Slc27a1*, solute carrier family 27 member 1 encoding fatty acid transport protein 1 (FATP1); *Slc27a6*, solute carrier family 27 member 6, encoding FATP6.



Extended Data Fig. 5 | See next page for caption.

Extended Data Fig. 5 | Co-culture models of neuron-astrocyte interaction in human brain lipid metabolism. (a) Protocol used for generation of human astrocytes (iAs) from induced pluripotent stem cells (hiPSCs). (b) Representative immunofluorescence images of human iAs of the indicated *SORT1* and *APOE* genotypes visualized for native mCherry, encoded by the viral transduction constructs (red), and immunostained for glial fibrillary acidic protein (GFAP, green) or S100 calcium-binding protein B (S100 β , green). Scale bars: 50 μ m and 150 μ m, respectively. Individual stainings were replicated in samples from 2-8 differentiation experiments. (c) RT-qPCR analysis of selected astrocyte marker genes in human iAs of the indicated *SORT1* and *APOE* genotypes (day 21 of culture). Individual biological replicates (n = 3 for E3WT, n = 5 for E3KO, n = 6 for E4WT and E4KO) from 2-3 individual differentiation experiments as well as mean \pm s.d. of the entire genotype group are shown. Statistical significance of data was tested using two-way ANOVA with Tukey's multiple comparison test. *ALDH1L1*, aldehyde dehydrogenase family 1 member L1; *S100B*, S100 calcium binding protein beta. (d) Levels of secreted apoE isoforms were determined in 30 μ l cell supernatant of human iAs (day 21 of culture) using western blotting. Recombinant human apoE (rec apoE, 12.5 ng) served as detection control. Comparative analyses with similar results were reproduced in 2-3 differentiation experiments. (e) Protocol used for generation of hiPSC-derived human neurons (iNs) in co-culture with mouse primary glia. (f) Representative

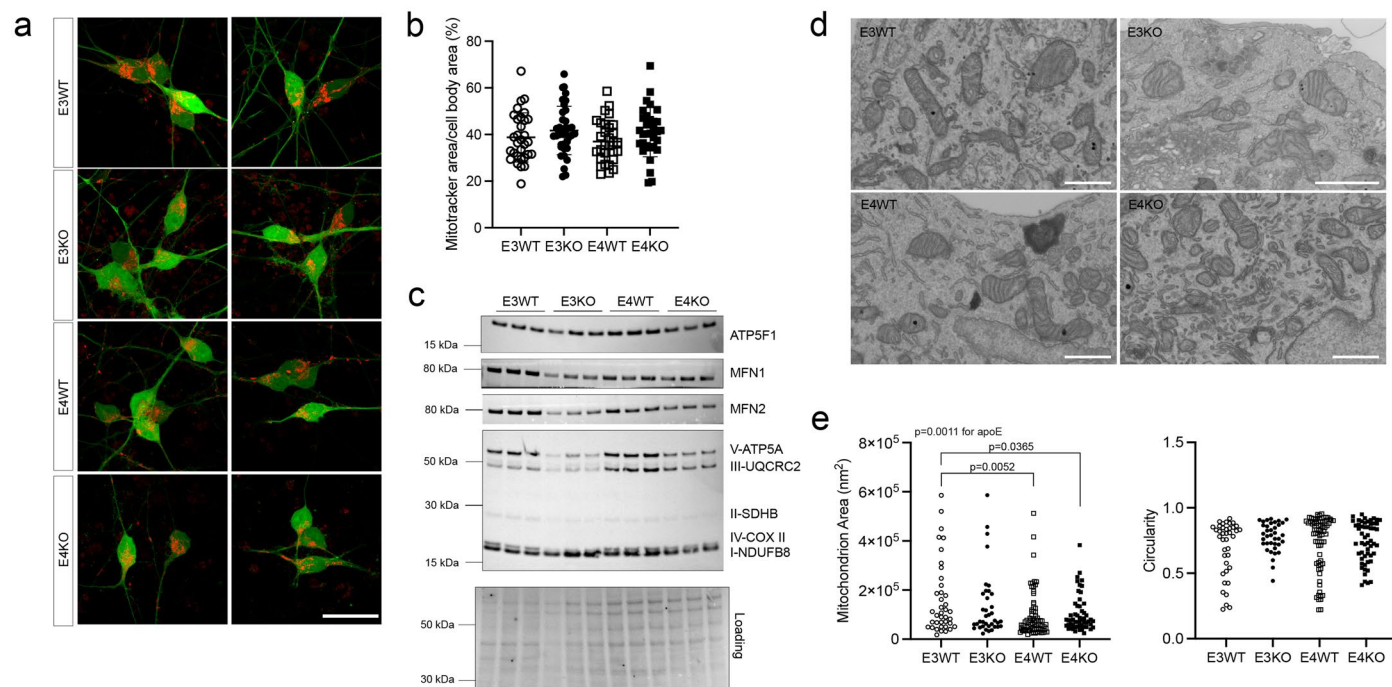
immunofluorescence images of human iNs of the indicated *SORT1* and *APOE* genotypes generated in co-culture with mouse primary glia (day 12 of culture). Neurons were visualized for native green fluorescent protein (GFP, green) and immunostained for microtubule associated protein 2 (MAP2, white) and sortilin (red). Cells were counterstained with DAPI (blue, in the merged images). Stainings were reproduced 2 - 5 times. Scale bar: 25 μ m. (g) Protocol used to generate hiPSC-derived human neurons (iNs) by addition of iAs-conditioned medium (iAsCM). (h) Representative immunofluorescence images of human iNs of the indicated *SORT1* and *APOE* genotypes grown in the presence of iAsCM (day 12 of culture). Neurons were visualized for native GFP (green) and immunostained for MAP2 (white) and sortilin (red). Neurons were counterstained with DAPI (blue, in the merged images). Scale bar: 25 μ m. Staining were replicated 2-9 times. (i) RT-qPCR analysis of selected neuronal marker genes in human iNs of the indicated *SORT1* and *APOE* genotypes (day 7 of culture). Individual biological replicates (n = 5) of three individual differentiation experiments, as well as mean \pm s.d. of the entire genotype group are shown. Statistical significance of data was tested using two-way ANOVA with Tukey's multiple comparison test. *MAP2*, microtubule associated protein 2; *NEFL*, neurofilament light chain; *TUBB3*, class III beta tubulin; *RBFOX3*, RNA binding Fox-1 homolog 3.



Extended Data Fig. 6 | See next page for caption.

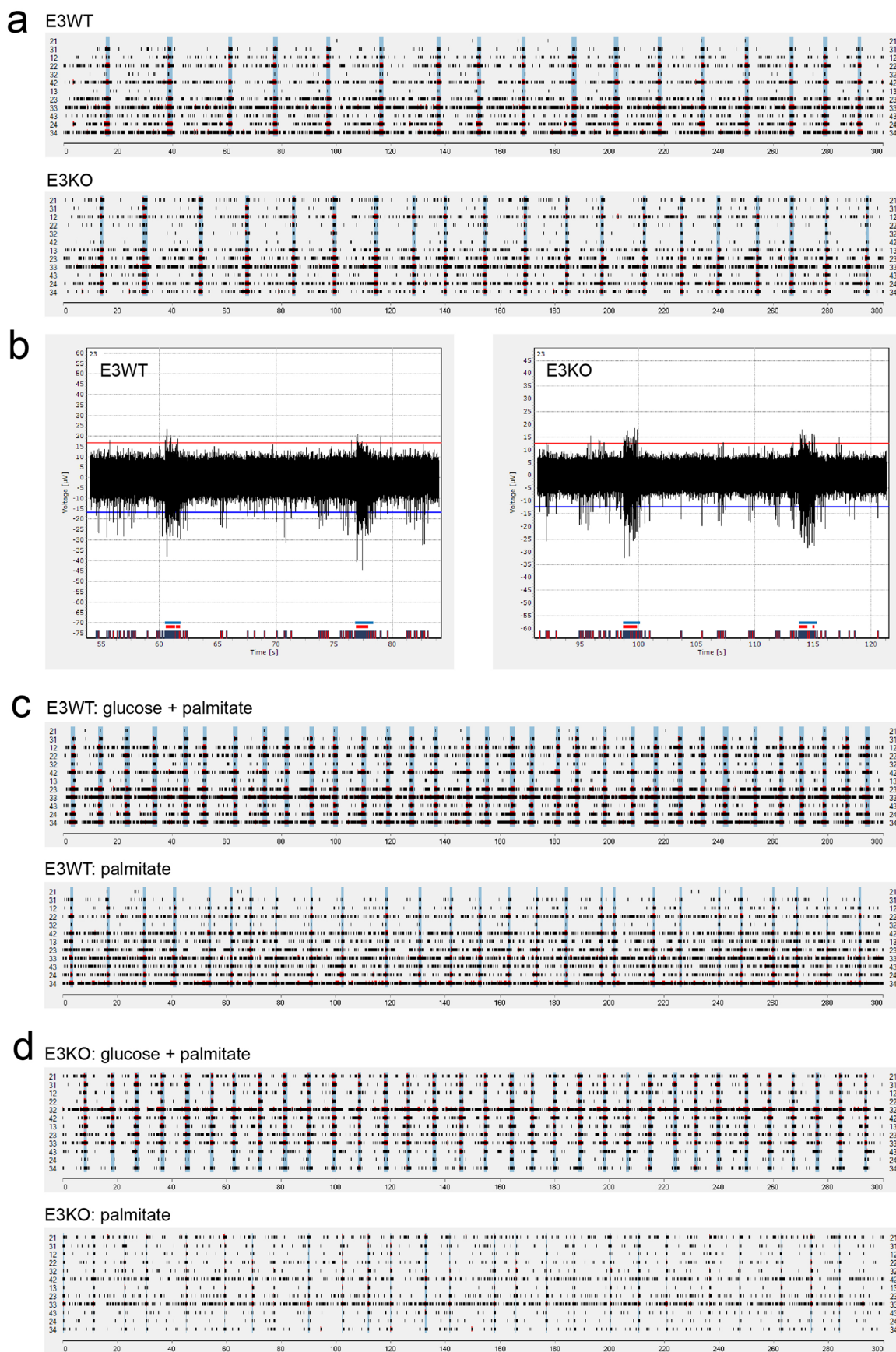
Extended Data Fig. 6 | Impact of *Sort1* genotypes on sensitivity of human neurons to etomoxir in 2nd *APOE3* iPSC line. (a) *APOE* genotyping of human iPSC cell (hiPSC) lines using RT-qPCR. The scatter plot X- and Y-axes represent allele discrimination for *APOE3* and *APOE4* genotypes. Shown hiPSC lines (colored squares) are *APOE3* (E3*) and either wildtype (WT) or genetically deficient for *SORT1* (KO). As internal controls, human samples being *APOE3/e3* (orange dot), *APOE3/e4* (grey dot), or *APOE4/e4* (yellow dot) were included in the genotyping. The white dot represents the water-only control. (b) Genome sequence analysis of the *SORT1* gene region in genome edited iPSC line E3*. Cell line E3*KO carries a 2 base pair deletion (yellow) downstream of the start ATG (green) as compared to the isogenic E3*WT control line. Sequences were aligned to the human *SORT1* reference sequence (NCBI: [FJ525881.1](https://www.ncbi.nlm.nih.gov/nuccore/FJ525881.1)). (c) Western blot analyses of lysates from the indicated iPSC lines, documenting the presence of sortilin in E3*WT, but absence of protein from lines E3*KO. Detection of GAPDH served as loading control. Analyses were reproduced at least twice. (d) Transcript levels of 94 genes involved in pluripotency and lineage differentiation potential were quantified in two independent replicates of iPSC lines E3*WT and E3*KO. Expression levels are shown as heatmap with colors correlating to the fold change in expression of the indicated gene relative to the undifferentiated reference set. (e) Box plot depicting transcript levels of genes in the Scorecard Assay panel in (d) associated with self-renewal or ectodermal, mesodermal or endodermal differentiation in iPSC lines of the indicated genotypes. Sample scores are plotted in color. Gray box and whisker plots (e) represent undifferentiated reference datasets (manufacturer-defined values). Scores close to 0 indicate similarity to the

reference set, scores greater than about 1 indicate upregulation and scores less than -1 indicate downregulation relative to the reference set. (f) Transcript levels of *OCT4* and *SOX2* in E3*WT and E3*KO iPSC lines were tested using RT-qPCR. For each line, data of 6 individual biological replicates as well as mean \pm s.d. of the entire data set are given. (g) Representative immunofluorescence images of E3*WT and E3*KO iNs (day 12 of culture) visualized for native GFP (green, in merged) and immunostained for MAP2 (white) and sortilin (red). Scale bar: 25 μ m. (h) RT-qPCR analysis of selected neuronal marker genes in human E3*WT and E3*KO iNs (day 8 of culture). Individual biological replicates ($n = 6$) from one differentiation experiment as well as mean \pm s.d. of the entire genotype group are shown. (i-j) Real-time oxygen consumption rates (OCR) were determined in the *APOE3/e3* iPSC line E3*, either WT (i) or KO (j) for *SORT1*. OCR was measured under basal conditions (0 - 20 min) and following sequential addition of oligomycin, carbonyl cyanide-p-trifluoromethoxyphenylhydrazone (FCCP), as well as rotenone and antimycin A (R/A). In addition, neurons had been treated with solvent control buffer or solutions containing 8 μ M UK5099 or 16 μ M etomoxir at the indicated time points (inhibitor). For each genotype, one exemplary experiment is shown to the left as well as the quantification of percentage of maximal OCR as compared to the control buffer treatment of the same genotype for the entire data set (set to 100%). Data represent the mean \pm s.d. of $n = 3$ biological replicates. Each biological replicate is the mean of $n = 10-16$ technical replicates. Statistical significance of data was tested using unpaired Student's *t* test (two-tailed). Individual respiratory profiles for three independent experiment are given in supplementary figure S9.



Extended Data Fig. 7 | Structural analyses of mitochondria in iPSC-derived human neurons. (a) Representative fluorescence images of human neurons of the indicated genotypes (day 7 of culture) depicting native fluorescence for GFP (green) as well as MitoTracker Red CMXRos (red). Scale bar: 25 μ m. This experiment was repeated in two independent differentiations. (b) Quantification of MitoTracker Red CMXRos-positive cell area (expressed as percentage of the total soma area) in human neurons. Data points represent individual cell measurements ($n = 31$ for E3WT, $n = 37$ for E3KO, $n = 30$ for E4WT, $n = 32$ for E4KO) from two differentiation experiments. Individual data points as well as mean \pm s.d. of the entire genotype group are shown. (c) Levels of the indicated respiratory chain subunits and mitofusins (MFN1 and MFN2) were determined in 5 μ g of total lysates from human neurons of the indicated *SORT1* and *APOE*

genotypes using western blotting (day 7 of culture). Staining of the membrane for total protein (No-StainTM, Thermo Fisher) served as equal loading and transfer control. The experiment was replicated in two independent differentiation experiments. (d) Representative electron microscopic images of mitochondria in human neurons of the indicated *SORT1* and *APOE* genotypes from one differentiation experiment. Scale bars: 730 nm or 1 μ m (E3KO). (e) Morphometric analyses of area and circularity of mitochondria, as deduced from electron microscopic images exemplified in (d). A subtle effect of *APOE* genotype on area is seen, but no impact of *SORT1* genotype nor interaction between *APOE* and *SORT1* on these parameters. A total of 39-78 mitochondria from 5-6 images per genotype were analyzed. Statistical significance of data was tested using two-way ANOVA with Tukey's multiple comparison test.

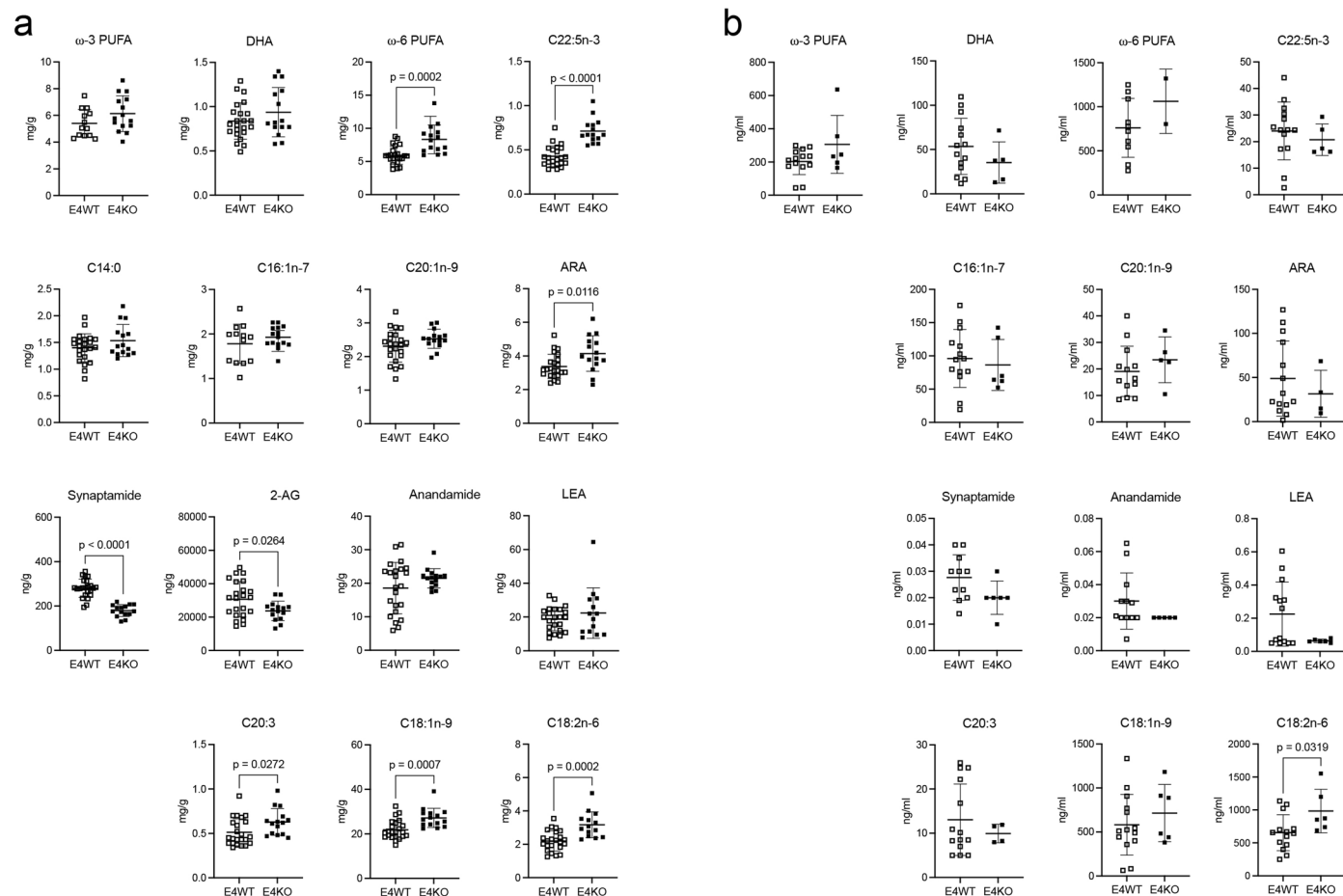


Extended Data Fig. 8 | See next page for caption.

Extended Data Fig. 8 | Electrical activity of E3*WT and E3*KO induced neurons.

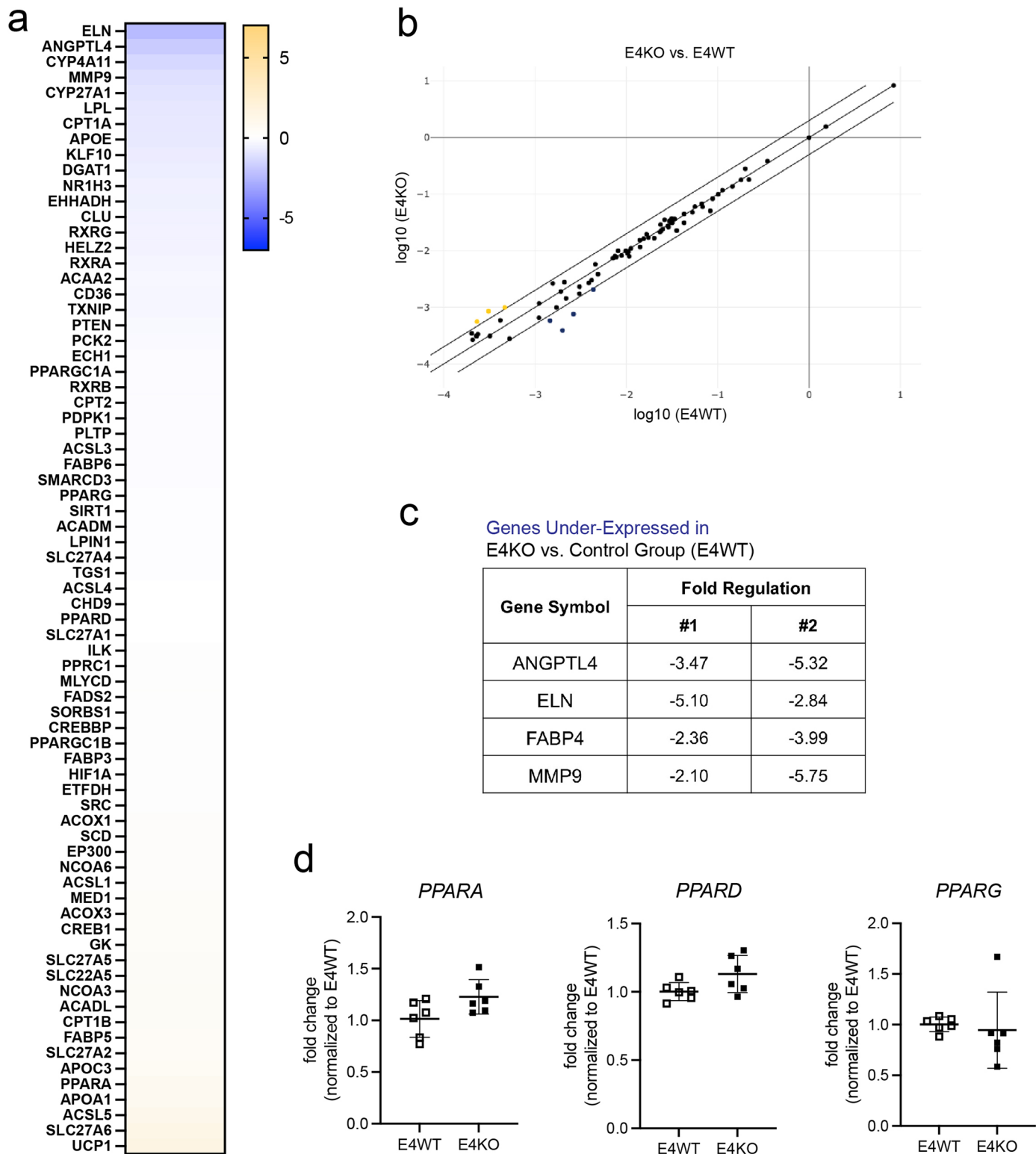
(a) Spontaneous electrical activity of E3*WT and E3*KO iNs (day 37 of culture) as recorded using multiple electrode arrays (MEA). Exemplary raster plots from a 5 min recording of one representative well are shown for each genotype. Each trace depicts one of twelve channels (with channel IDs indicated on the y-axis) in a representative well. The x-axis indicates time in seconds. Each black line represents a single spike. Red lines indicate channel bursts, while blue lines

represent network burst detections. (b) Representative single-channel traces showing spontaneous electrical activity over time (30 s) in E3*WT and E3*KO iNs. (c-d) Exemplary 5 min MEA recordings of electrical activity of one representative well each for E3*WT (c) and E3*KO (d) iNs, comparing cells treated with palmitate in the presence of glucose (pre-treatment: glucose + palmitate) and after 48 h of glucose deprivation (palmitate).



Extended Data Fig. 9 | Sortilin deficiency does not impact poly-unsaturated fatty acid levels in human apoE4 neurons. (a) Concentrations of selected lipids in iPSC-derived cortical neurons were determined using LC-MS. Neurons (day 12 of culture) were *APOE4/ε4* and either wildtype (E4WT) or, genetically deficient for *SORT1* (E4KO). Data from individual biological replicates ($n = 13 - 23$ for E4WT, $n = 15$ for E4KO) of 2 - 4 individual differentiation experiments are given. (b) Concentrations of selected lipids in the cell supernatant of iPSC-derived E4WT and E4KO astrocytes (days 21 - 29 of culture) were determined using LC-MS.

Individual biological replicates ($n = 2 - 14$, depending on the analyzed lipid) of 2 - 6 individual differentiation experiments are shown. Individual data points as well as mean \pm s.d. of the entire genotype group are given. Statistical significance of data was tested using unpaired Student's *t* test (two-tailed). No statistical test was performed for ω -6 fatty acids level ($n = 2$ for E4KO). ARA, arachidonic acid; 2-AG, 2-arachidonoylglycerol; DHA, docosahexaenoic acid; LEA, linoleoyl ethanolamide; PUFA, poly-unsaturated fatty acid.



Extended Data Fig. 10 | See next page for caption.

Extended Data Fig. 10 | Sortilin deficiency does not impact PPAR-dependent gene expression in human apoE4 neurons. Expression levels of 84 peroxisome proliferator-activated receptor (PPAR) target genes were determined in iPSC-derived human neurons treated with astrocyte-conditioned media using the human PPAR Targets RT2 Profiler PCR Array. Neurons (day 12 of culture) were *APOE4/ε4* and either wildtype (E4WT) or genetically deficient for *SORT1* (E4KO). One exemplary experiment (from two independent experiments) is shown. (a) Expression levels are given as heat map with transcript levels in E4KO presented as log₂ fold change as compared to E4WT (set to 0). Blue and yellow color spectra indicate down-regulated or up-regulated genes, respectively. (b) Scatterplot analysis comparing log₂-transformed relative expression for all tested PPAR target genes in E4WT and E4KO neurons. The center diagonal line indicates

unchanged gene expression levels. The outer diagonal lines indicate 2-fold regulation threshold. Genes with >2-fold difference in transcript level between groups are presented as blue and yellow dots, indicating down- or up-regulated genes, respectively. (c) Selected list of genes downregulated by >2 fold in E4KO as compared to E4WT human neurons treated with iAs-conditioned media. One exemplary experiment (from two independent differentiation experiments) is shown. (d) RT-qPCR analysis of selected PPAR target genes in E4WT and E4KO human neurons treated with iAs-conditioned media (day 12 of culture). Data points for n = 6 biological replicates (from two differentiations) as well as mean ± s.d. are given. No statistical difference comparing genotypes was seen using unpaired Student's t test (two-tailed).

Reporting Summary

Nature Portfolio wishes to improve the reproducibility of the work that we publish. This form provides structure for consistency and transparency in reporting. For further information on Nature Portfolio policies, see our [Editorial Policies](#) and the [Editorial Policy Checklist](#).

Statistics

For all statistical analyses, confirm that the following items are present in the figure legend, table legend, main text, or Methods section.

- | n/a | Confirmed |
|-------------------------------------|--|
| <input type="checkbox"/> | <input checked="" type="checkbox"/> The exact sample size (n) for each experimental group/condition, given as a discrete number and unit of measurement |
| <input type="checkbox"/> | <input checked="" type="checkbox"/> A statement on whether measurements were taken from distinct samples or whether the same sample was measured repeatedly |
| <input type="checkbox"/> | <input checked="" type="checkbox"/> The statistical test(s) used AND whether they are one- or two-sided
<i>Only common tests should be described solely by name; describe more complex techniques in the Methods section.</i> |
| <input checked="" type="checkbox"/> | <input type="checkbox"/> A description of all covariates tested |
| <input type="checkbox"/> | <input checked="" type="checkbox"/> A description of any assumptions or corrections, such as tests of normality and adjustment for multiple comparisons |
| <input type="checkbox"/> | <input checked="" type="checkbox"/> A full description of the statistical parameters including central tendency (e.g. means) or other basic estimates (e.g. regression coefficient) AND variation (e.g. standard deviation) or associated estimates of uncertainty (e.g. confidence intervals) |
| <input checked="" type="checkbox"/> | <input type="checkbox"/> For null hypothesis testing, the test statistic (e.g. F , t , r) with confidence intervals, effect sizes, degrees of freedom and P value noted
<i>Give P values as exact values whenever suitable.</i> |
| <input checked="" type="checkbox"/> | <input type="checkbox"/> For Bayesian analysis, information on the choice of priors and Markov chain Monte Carlo settings |
| <input checked="" type="checkbox"/> | <input type="checkbox"/> For hierarchical and complex designs, identification of the appropriate level for tests and full reporting of outcomes |
| <input checked="" type="checkbox"/> | <input type="checkbox"/> Estimates of effect sizes (e.g. Cohen's d , Pearson's r), indicating how they were calculated |

Our web collection on [statistics for biologists](#) contains articles on many of the points above.

Software and code

Policy information about [availability of computer code](#)

Data collection

Confocal images were acquired with Zeiss Zen software (v2.6). Bioenergetic experiments were generated using Seahorse Wave Desktop Software v2.6.1 (Agilent) and Cytation 5 (BioTek Instrument). Western blot membranes were visualized using iBright Analysis software (v1.8.1). qRT-PCR data was acquired with QuantStudio Real-Time PCR software (v1.3). Confocal images were acquired on Zeiss LSM780 or Zeiss LSM800 confocal microscopes. Cell sorting was performed with BD Aria Fusion. Metabolomics raw data were processed in Bruker Compass TargetAnalysis (v3.1). MEA data were acquired with Multi Channels Systems (v2.0.11.0). Electron microscopy: MAPS software package (v3.27).

Data analysis

Image analysis: Fiji Image J (v2.14.0); Statistics: Prism (v10); Bioenergetic experiments: Agilent Seahorse Wave Desktop Software v2.6.1; General expression data analysis: ThermoFisher Cloud (web-based analysis platform), Qiagen GeneGlobe (web-based analysis platform); Metabolomics data analysis: Bruker Compass DataAnalysis (4.1). MEA data analysis: Multi Channel Analyzer (Multi Channel Systems, v 2.0.6.0).

For manuscripts utilizing custom algorithms or software that are central to the research but not yet described in published literature, software must be made available to editors and reviewers. We strongly encourage code deposition in a community repository (e.g. GitHub). See the Nature Portfolio [guidelines for submitting code & software](#) for further information.

Data

Policy information about [availability of data](#)

All manuscripts must include a [data availability statement](#). This statement should provide the following information, where applicable:

- Accession codes, unique identifiers, or web links for publicly available datasets
- A description of any restrictions on data availability
- For clinical datasets or third party data, please ensure that the statement adheres to our [policy](#)

All data supporting the findings of this study are available from the corresponding author upon request. All data presented in the manuscript are provided as source data files.

Research involving human participants, their data, or biological material

Policy information about studies with [human participants or human data](#). See also policy information about [sex, gender \(identity/presentation\), and sexual orientation](#) and [race, ethnicity and racism](#).

Reporting on sex and gender	Not applicable.
Reporting on race, ethnicity, or other socially relevant groupings	Not applicable.
Population characteristics	Not applicable.
Recruitment	Not applicable.
Ethics oversight	Not applicable.

Note that full information on the approval of the study protocol must also be provided in the manuscript.

Field-specific reporting

Please select the one below that is the best fit for your research. If you are not sure, read the appropriate sections before making your selection.

Life sciences Behavioural & social sciences Ecological, evolutionary & environmental sciences

For a reference copy of the document with all sections, see [nature.com/documents/nr-reporting-summary-flat.pdf](https://www.nature.com/documents/nr-reporting-summary-flat.pdf)

Life sciences study design

All studies must disclose on these points even when the disclosure is negative.

Sample size	No samples size calculations were performed. Sample size and biological replicates for each experiment were described in figure legends and were determined upon consideration of samples availability, duration of experiment and time needed for data processing.
Data exclusions	Data distribution was assumed to be normal. For certain experiments, data was tested for normal distribution and outliers were determined using Grubbs' test or the ROUT method (Q = 1%), while GraphPrism has been used to exclude outliers. In lipidomics, certain data points from one experiment were excluded because of technical discrepancies between experiments.
Replication	Most of experiments were replicated at least twice, with actual number of replicates given in respective figure legends.
Randomization	All animals and/or cell wells in in vitro study were randomly selected for sample collection and experimentation.
Blinding	For animal studies, the mice were assigned to different groups according to genotypes. The mice were age- and sex-matched between genotypes to minimize variance. The mice were randomly assigned to control and different treatment groups. All mice were given a number after birth and subsequent experiments were performed blind to genotype as much as possible. All cell culture wells for in vitro studies were collected and selected for analysis randomly.

Reporting for specific materials, systems and methods

We require information from authors about some types of materials, experimental systems and methods used in many studies. Here, indicate whether each material, system or method listed is relevant to your study. If you are not sure if a list item applies to your research, read the appropriate section before selecting a response.

Materials & experimental systems

n/a	Included in the study
<input type="checkbox"/>	<input checked="" type="checkbox"/> Antibodies
<input type="checkbox"/>	<input checked="" type="checkbox"/> Eukaryotic cell lines
<input checked="" type="checkbox"/>	<input type="checkbox"/> Palaeontology and archaeology
<input type="checkbox"/>	<input checked="" type="checkbox"/> Animals and other organisms
<input checked="" type="checkbox"/>	<input type="checkbox"/> Clinical data
<input checked="" type="checkbox"/>	<input type="checkbox"/> Dual use research of concern
<input checked="" type="checkbox"/>	<input type="checkbox"/> Plants

Methods

n/a	Included in the study
<input checked="" type="checkbox"/>	<input type="checkbox"/> ChIP-seq
<input checked="" type="checkbox"/>	<input type="checkbox"/> Flow cytometry
<input checked="" type="checkbox"/>	<input type="checkbox"/> MRI-based neuroimaging

Antibodies

Antibodies used

anti-APOE (Millipore, #AB947)
 anti-ATP5F1 (Proteintech, #68304-1-Ig)
 anti-CPT1A (8F6AE9) (Abcam, #ab128568)
 anti-FABP6 (Proteintech, #13781-1-AP)
 anti-FABP7 (Sigma-Aldrich, #ABN14)
 anti-GAPDH (Millipore, #374)
 anti-GFAP (Abcam, #ab53554)
 anti-MAP2 (Synaptic Systems, #188 004)
 anti-MFN1 (3F11C11) (Proteintech, # 66776-1-Ig)
 anti-MFN2 (7H42L13) (Invitrogen, #702768)
 anti-MTCO1 (1D6E1A8) (Invitrogen, #459600)
 anti-NANOG (R&D Systems, #AF1997)
 anti-OCT4 (clone 3A2A20) (StemCell, #60093)
 anti-S100 (DAKO, #GA504)
 anti-sortilin (for IF: R&D #AF3154, for WB: BD Biosciences #612101)
 anti-SOX2 (clone 245610, #MAB2018)
 anti-SSEA4 (MC813-70) (Abcam, #16287)
 Total OXPPOS Human WB antibody cocktail (Abcam, #ab110411)
 Total OXPPOS Rodent WB antibody cocktail (Abcam, #STN-19467)

Validation

anti-APOE (Millipore, #AB947): https://www.merckmillipore.com/DK/en/product/Anti-Apolipoprotein-E-Antibody,MM_NF-AB947
 anti-ATP5F1 (Proteintech, #68304-1-Ig): <https://www.ptglab.com/products/ATP5F1-Antibody-68304-1-Ig.htm>
 anti-CPT1A (8F6AE9) (Abcam, #ab128568): <https://www.abcam.com/products/primary-antibodies/cpt1a-antibody-8f6ae9-ab128568.html>
 anti-FABP3 (Proteintech, #10676-1-AP): <https://www.ptglab.com/products/FABP3-Antibody-10676-1-AP.htm>
 anti-FABP5 (BioVendor, #RD181060100): <https://www.biovendor.com/epidermal-fatty-acid-binding-protein-human-rabbit-polyclonal-antibody>
 anti-FABP6 (Proteintech, #13781-1-AP): <https://www.ptglab.com/products/FABP6-Antibody-13781-1-AP.htm>
 anti-FABP7 (Sigma-Aldrich, #ABN14): https://www.merckmillipore.com/DK/en/product/Anti-Brain-lipid-binding-protein-Antibody,MM_NF-ABN14
 anti-GAPDH (Millipore, #MAB374): https://www.merckmillipore.com/DK/en/product/Anti-Glyceraldehyde-3-Phosphate-Dehydrogenase-Antibody-clone-6C5,MM_NF-MAB374
 anti-GFAP (Abcam, #ab53554): <https://www.abcam.com/products/primary-antibodies/gfap-antibody-ab53554.html>
 anti-MAP2 (Synaptic Systems, #188 004): <https://www.sysy.com/product/188004#list>
 anti-MFN1 (3F11C11) (Proteintech, # 66776-1-Ig): <https://www.ptglab.com/products/MFN1-Antibody-66776-1-Ig.htm>
 anti-MFN2 (7H42L13) (Invitrogen, #702768): <https://www.thermofisher.com/antibody/product/MFN2-Antibody-clone-7H42L13-Recombinant-Monoclonal/702768>
 anti-MTCO1 (1D6E1A8) (Invitrogen, #459600): <https://www.thermofisher.com/antibody/product/MTCO1-Antibody-clone-1D6E1A8-Monoclonal/459600>
 anti-NANOG (R&D Systems, #AF1997): https://www.rndsystems.com/products/human-nanog-antibody_af1997
 anti-OCT4 (clone 3A2A20) (StemCell, #60093): <https://www.stemcell.com/products/anti-human-oct4-oct3-antibody-clone-3a2a20.html>
 anti-S100 (DAKO, #GA504): <https://www.agilent.com/en/product/immunohistochemistry/antibodies-controls/primary-antibodies/s100-%28dako-omnis%29-76198>

anti-sortilin antibodies were additionally validated in this study by gene knockdown in mice model and in hiPSCs (for IF: https://www.rndsystems.com/products/human-sortilin-antibody_af3154, for WB: <https://www.bdbiosciences.com/ko-kr/products/reagents/western-blotting-and-molecular-reagents/western-blot-reagents/purified-mouse-anti-neurotensin-receptor-3.612101>)

anti-SOX2 (clone 245610, #MAB2018): https://www.rndsystems.com/products/human-mouse-rat-sox2-antibody-245610_mab2018
 anti-SSEA4 (Abcam, #16287): <https://www.abcam.com/en-an/products/primary-antibodies/ssea4-antibody-mc813-70-ab16287>
 Total OXPPOS Human WB antibody cocktail (Abcam, #ab110411): <https://www.abcam.com/products/panels/total-oxphos-human-wb-antibody-cocktail-ab110411.html>
 Total OXPPOS Rodent WB antibody cocktail (Abcam, #STN-19467): antibody under this catalog number was discontinued (available as Abcam #ab110413)
 anti-VIM (clone V9) (DAKO, #M0725): <https://www.agilent.com/cs/library/packageinsert/public/103621002.PDF>

Eukaryotic cell lines

Policy information about [cell lines and Sex and Gender in Research](#)

Cell line source(s)	Human induced human pluripotent stem cell lines (BIHi005-A (https://hpscereg.eu/cell-line/BIHi005-A), WTSii009-A (https://hpscereg.eu/cell-line/WTSii009-A) and BIHi043(MDCI-053-A-49; https://hpscereg.eu/cell-line/HMGUi001-A)) were obtained from the MDC Technology Platform Pluripotent Stem Cells (in-house) or the Wellcome Trust Sanger Institute.
Authentication	Cell lines were quality-controlled for genome stability and pluripotency, and verified for APOE and SORT1 genotypes as described in method section.
Mycoplasma contamination	All cell lines were routinely tested negative for mycoplasma.
Commonly misidentified lines (See ICLAC register)	No such line lines were used in this study.

Animals and other research organisms

Policy information about [studies involving animals](#); [ARRIVE guidelines](#) recommended for reporting animal research, and [Sex and Gender in Research](#)

Laboratory animals	All animal procedures were conducted in accordance to local ethics committees approval (X9017/17). Experiments were conducted in male 12-weeks old mice on an inbred C57Bl6/J background. The animals were kept on normal chow (4.5% crude fat, 39% carbohydrates).
Wild animals	No wild animals were used in the study.
Reporting on sex	Studies were conducted in male and female mice.
Field-collected samples	No samples collected from the field were used in the study.
Ethics oversight	All animal procedures were conducted in accordance with local ethics committees approval (X9017/17) and overseen by institutional animal welfare officers.

Note that full information on the approval of the study protocol must also be provided in the manuscript.

Plants

Seed stocks	Not applicable.
Novel plant genotypes	Not applicable.
Authentication	Not applicable.